energies

MDPI

Article

Characterisation and Field Test of a Simple AvaSpec Array Spectroradiometer for Solar Irradiance Measurements at an Alpine Site

Olga Pisani [1,*,†], Henri Diémoz [2,*,†] and Claudio Cassardo [1]

[1] Physics Department, University of Turin, 10125 Turin, Italy
[2] ARPA Valle d'Aosta, 11020 Saint-Christophe, Italy
* Correspondence: olgapisani.97@gmail.com (O.P.); h.diemoz@arpa.vda.it (H.D.); Tel.: +39-165-278576 (H.D.)
† These authors contributed equally to this work.

Abstract: Array spectroradiometers are increasingly being used to measure natural and artificial optical radiation because of their many advantages compared to traditional instruments. This study aims to thoroughly characterise a commercially available, cost-effective array device (AvaSpec ULS2048-LTEC) and compare its measurements of global solar irradiance in the 290–1100 nm wavelength range with those collected during three short-term field campaigns from more advanced, or specifically designed instruments. Moreover, the AvaSpec observations were compared with the output of a radiative transfer model. The results show that, despite its conceptually simple instrumental design, the AvaSpec can provide measurements of nearly comparable quality to those from reference instruments (e.g., UV index and global horizontal irradiance generally within ±5%) if all corrections are performed. These preliminary observations will be the basis of a long-term series at the Aosta–Saint-Christophe observatory, which can be employed to study solar energy production, biological effects and atmospheric composition changes in the Alpine environment. All procedures, including the encountered issues and proposed solutions, are described in detail.

Keywords: solar energy; solar radiation; array spectroradiometer; UV index; global spectral irradiance; instrumental characterisation; radiative transfer models

Citation: Pisani, O.; Diémoz, H.; Cassardo, C. Characterisation and Field Test of a Simple AvaSpec Array Spectroradiometer for Solar Irradiance Measurements at an Alpine Site. *Energies* **2023**, *16*, 2998. https://doi.org/10.3390/en16072998

Academic Editor: Juan Luis Bosch Saldaña

Received: 27 January 2023
Revised: 20 March 2023
Accepted: 21 March 2023
Published: 24 March 2023

1. Introduction

Array spectroradiometers are emerging instruments for the monitoring of radiation from the sun or from artificial sources in the ultraviolet (UV, wavelength < 400 nm), visible and infrared (IR, wavelength > 780 nm) bands. Contrary to the more conventional scanning spectroradiometers, which sequentially sample different wavelengths by means of moving components, array devices project the light diffracted by a dispersing element onto a series of detectors where the spectrum is recorded nearly instantaneously over a wide wavelength interval [1]. This provides useful information on atmospheric radiative transfer and solar energy reaching the Earth's surface in rapidly changing conditions [2]. Furthermore, owing to their compactness, they are portable and robust and can be carried on unconventional platforms, such as ships, aeroplanes or unmanned aerial vehicles [3]. The increased radiometric stability of their solid-state detectors, compared to the photomultiplier tubes usually employed in traditional instruments, and their affordable cost are additional significant assets.

Hence, unsurprisingly, array spectroradiometers have been operated for a great variety of applications. One example is their use in monitoring the performances of photovoltaic (PV) cells. Indeed, spectrally resolved solar irradiance measurements over a wide wavelength range are crucial for identifying and understanding the atmospheric and environmental factors, such as clouds, aerosols and precipitable water, influencing the instantaneous and predicted (in both the short and long term) PV power output [4–8].

Technical issues, such as panel ageing, temperature and the deposition of dust and snow [9–11], also affect panel performances in real conditions, and their effects can be detected by concurrent monitoring of solar radiation. Further details on the application of spectroradiometers to PV technology are provided in Section S1 of the Supplementary Materials. Array spectroradiometers are also adopted in studies about air quality, photochemistry and atmospheric composition [12–21], by taking advantage of the spectral signature of some light-absorbing atmospheric compounds; phototherapy and medical dosimetry [22,23], in which the observation of the radiation spectrum is essential for assessing wavelength-dependent biological effects; measurement of the Earth's surface reflectance, e.g., to identify snow impurities [24]; and the monitoring of water quality and ecosystems [25–27]. Finally, array systems are not only useful in research but may also be introduced in industrial applications where reference solar spectra are required [28] or where spectroscopy-based techniques are employed for process control [29]. Additional examples are provided in Section S1.

Despite the aforementioned advantages of the array-based technology, the simpler design of such instruments compared to scanning spectroradiometers exposes them to more evident instrumental artefacts, one above all straylight, due to the adoption of a single monochromator [22,23,30,31]. This must be compensated for by a greater effort from the operator's side to post-correct the signal or to carefully customise an instrument to mitigate these effects.

The aim of the present study is to test a commercially available array spectroradiometer (AvaSpec ULS2048-LTEC) in order to answer the following research questions:

1. Can a single array spectroradiometer make reliable measurements of global irradiance in a wide spectral range, encompassing UV, visible and near-IR wavelengths simultaneously?

   Previous research with array spectroradiometers has often focused on specific regions of the spectrum, such as the UV range, in which accurate measurements are challenging owing to the steep spectral gradient of the solar irradiance, or outside this interval, e.g., for applications of energy production (see Table S1 for a non-exhaustive list of previous studies involving array spectroradiometers). A novel aspect of the present work is the fact that we did not focus on a particular spectral region. Instead, we compared the results from the AvaSpec with reference observations in several wavelength ranges.

2. What minimal procedures are required to characterise and calibrate the AvaSpec and obtain measurements of satisfactory quality?

   Several studies have tackled the characterisation/calibration topic based on sophisticated methods and equipment, e.g., [32]. Conversely, here we tried to keep our instrumental and laboratory setup as simple and affordable as possible. This allows other operators interested in starting similar monitoring programs to easily replicate our results without the need for cutting-edge technology (e.g., tunable lasers).

3. How good is the agreement between the AvaSpec measurements and the radiative transfer model (RTM) simulations?

   We performed the spectral simulations with an RTM, providing as input the available ancillary information from co-located instruments. The synthetic spectra were then compared with measurements from the array spectroradiometer. They were also used to compensate the AvaSpec measurements for the unmeasured component of the solar spectrum.

4. What are the strengths of the new system compared to the existing reference instruments?

Another distinctive feature of this study is represented by the geographical context considered here, which is an Alpine region characterised by complex orography. Due to the high average altitude of the domain, generally low atmospheric pollution and the presence of snow on the mountains, peak irradiances are expected in the area around the

observatory and at other sites where the instrument could be deployed in the future. This impacts renewable energy production [33], hydropower through accelerated meltwater from seasonal snow [34], radiative balance both at the surface [35] and along the vertical profile [36] and the enhanced effects on humans and ecosystems [37,38]. Hence, solar radiation is an important variable to be monitored in the fragile mountain environment, notably in the context of a changing climate [39–42], and for public health purposes. Finally, space-based estimates of solar radiation are challenging over complex orography [43–45] and measurements over mountainous areas are essential for providing ground truth data. Nonetheless, continuous and accurate observations of solar radiation in such places are less common than over flat terrain.

The paper has the following structure. Section 2 describes the measurement site and instruments; Section 3 explains the methods for characterising the spectroradiometer in the laboratory and for post-correcting its measurements, including the use of radiative models to extend the available information to a wider spectral range; and Section 4 shows the outcome of the characterisation and the results of the first field measurements. A discussion on the quality of the measurements and the main issues encountered is included in Section 5. Conclusions are drawn in Section 6.

2. Measurement Site and Instruments

2.1. The Aosta–Saint-Christophe Observatory

This study was carried out in the Aosta Valley, a region in the northwestern Italian Alps (Figure 1a) at the border with France and Switzerland. The region, which is about 80×40 km^2 wide, features the typical characteristics of a mountain environment, such as high elevation (average $>$ 2000 m a.s.l., with a peak value of 4808 m a.s.l., corresponding to the top of Mont Blanc, Figure 1b) and generally pristine atmosphere. A solar measurement network is managed by the local Environmental Protection Agency (ARPA) in the region and consists of remote stations, located at altitudes between 1640 and 3500 m a.s.l. and equipped with broadband UV radiometers [37,38], and a main observatory at the agency headquarters in Aosta–Saint-Christophe. The latter is situated at the bottom of the valley (560 m a.s.l., 45.74° N, 7.35° E, WMO Integrated Global Observing System ID 0-380-5-1), in a semi-rural environment, marginally influenced by emissions from the small urban settlement of Aosta (34,000 inhabitants) and from the Po Basin (about 100 km to the southeast) [46]. Although mountains as high as 3500 m a.s.l. dominate the observatory, which also impacts the effective albedo at the site in winter [47], the horizon there is rather wide, reaching maximum elevation angles of about 20° at the south of the station (Figure 1c). The array spectroradiometer, which is the focus of this study, was tested at the main observatory; however, we do not exclude future relocation to one of the remote sites.

Figure 1. (**a**) The Aosta Valley (coloured rectangle), in northwestern Italy. (**b**) A 3D view of the investigated area: the Aosta–Saint-Christophe observatory (blue marker), together with the geographical references of Mont Blanc (4808 m a.s.l., the highest mountain in the European Alps) and the Po Valley, extending from the southeastern side of the Aosta Valley to the most part of northern Italy. Images from Google Earth. (**c**) Local horizon and solar elevation angles during three days representative of the short-term campaigns (2022–2023).

2.2. Instruments

The experimental setup at the solar observatory includes both the tested array spectroradiometer (Section 2.2.1) and co-located state-of-the-art instruments for validation or providing ancillary information (Section 2.2.2). An optical laboratory, employed to characterise the array spectroradiometer, is also available at the facility (Section 2.2.3).

2.2.1. Array Spectroradiometer

The instrument is based on a commercially available spectrometer (AvaSpec ULS2048-LTEC). Figure 2 is a schematic representation of the equipment. The optical bench (Figure 2d) is designed as a symmetrical Czerny–Turner monochromator with a 75 mm focal length. Light entering the instrument is collimated by a spherical mirror and diffracted by a plain grating (pitch 300 lines mm^{-1}, blazing at 500 nm). A second spherical mirror focuses the resulting light and projects it onto a charge-coupled device (CCD) linear detector array with 2048 pixels. The detector is thermoelectrically cooled in three stages at a selectable temperature (default 4.98 ± 0.08 °C). The current setup, employing a 10 µm entrance slit, allows measurements in the nominal range of 280–1100 nm with a spectral resolution of about 1 nm. While the wide spectral range of the instrument would seem to conflict with accurate observations in specific wavelength regions, it actually ensures that most of the straylight is in-band and can be post-corrected with mathematical methods (Section 3.1.3). Additionally, a diamond-like carbon (DLC) UV/VIS detector collection lens and an order-sorting coating (OSC) enhance the sensitivity at shorter wavelengths and reduce the effects of second-order refraction, respectively. The acquisition electronic, based on a 16-bit AD converter, supports integration times from 1.11 ms to 10 min. The dynamic range of the detector can be further broadened with the bracketing technique [23,48], i.e., by using different integration times and saturating the signal in some spectral regions while improving the signal-to-noise ratio in others (Section 3.2). The spectrometer operating software (Figure 2e) was developed in-house based on the manufacturer's programming libraries.

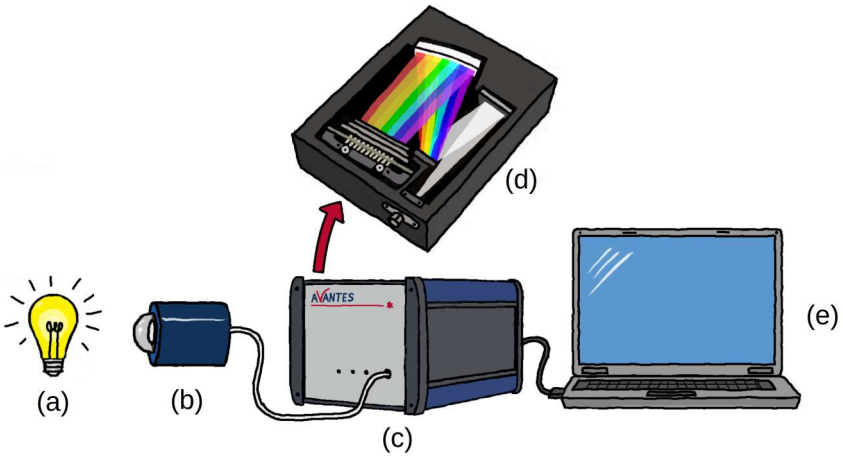

Figure 2. Schematic diagram of the equipment: (**a**) light source (e.g., calibration lamp or the sun) to be measured; (**b**) diffuser, enclosed in its case; (**c**) spectrometer case, which includes (**d**) monochromator/optical bench (figure adapted from www.avantes.com/support/theoretical-background/introduction-to-spectrometers/, accessed on 23 March 2023); (**e**) operating PC.

Whilst the detector is cooled, the temperature of the instrument board depends on the ambient conditions (Figure 2c). To reduce this dependence and avoid effects due to the temperature gradients inside the instrument, such as spectral shifts [49,50], we keep the spectrometer enclosed in a temperature-stabilised box (Bentham, Environmentally Controlled Enclosure). The nominal temperature in the box was initially set to the same temperature as the outer cabin (25 °C), and it stabilised at 30 °C. The large temperature

difference with respect to the detector may be the reason for some instabilities described later in the manuscript (Section 4.3). After the discovery of this issue, the temperature inside the box was decreased to 15 °C by setting a lower temperature in the controller as well.

The entrance optic (Figure 2b), collecting global irradiance from the upward hemisphere, consists of a high precision, environmentally sealed, cosine-corrected transmission diffuser (200–1100 nm) from Bentham (model D7). An ad hoc case was designed around the diffuser at the Physical Meteorological Observatory/World Radiation Centre (PMOD/WRC, Davos, Switzerland) to keep its temperature constant, thus avoiding variations in the Teflon transmittance [51] and moisture inside the diffuser (by using a desiccant cartridge). This optic is similar to that of our reference spectroradiometer (Section 2.2.2), which makes the comparison consistent between the irradiance measured by the two instruments (Figure 3). The diffuser is attached to the AvaSpec with a UV-grade fused silica fibre bundle (1 mm core diameter, 5 m length, 200–1350 nm transmittance range) of the multi-mode type to reduce the sensitivity of the fibre transmission to bending and torsion. The fibre terminates with an FC/PC connector to the instrument side, which ensures good reproducibility in the case of removal and reconnection.

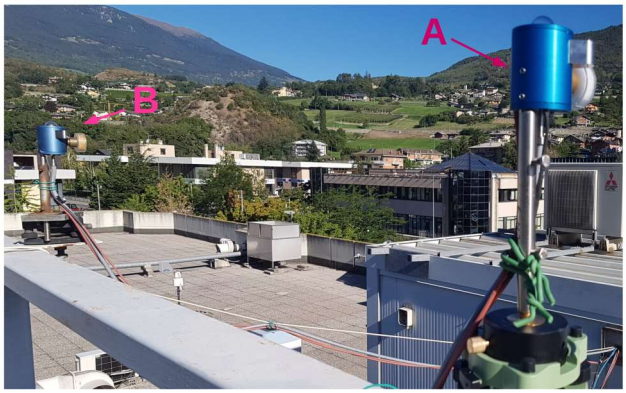

Figure 3. Entrance optics of the array spectroradiometer (**A**) and of the reference Bentham spectroradiometer (**B**). The two optics, both based on Bentham D7 global diffusers, are similar.

Neither the diffuser nor the spectrometer is equipped with a shutter. This choice was dictated by the intention to keep the instrument design simple and avoid some commonly experienced issues [52]. We found that this limitation can be partially overcome by an accurate pre-characterisation of the dark signal (Section 3.1), activation of blind pixel correction and thermoelectric cooling of the detector [50,52]. Additionally, this method has the advantage of speeding up the measurement process, as dark measurements can be avoided.

2.2.2. Co-Located Instrumentation

The reference instrument for global solar irradiance measurements in the UV-visible range is a Bentham DTMc300 scanning spectroradiometer [53], equipped with a double monochromator for better straylight rejection. The spectral scans are routinely performed in the range of 290—500 nm (no radiation reaches the Earth's surface at wavelengths < 290 nm at the selected location) with a step of 0.25 nm, spectral resolution of 0.54 nm and a frequency of one scan every 15 min. The duration of each acquisition is about 5 min, owing to the scanning nature of the spectroradiometer. The calibration procedures and the traceability chain of the Bentham are thoroughly described elsewhere [54]. The expanded (coverage factor $k = 2$) uncertainty of the spectral irradiance measurements is estimated to be 4% at wavelengths > 310 nm and solar zenith angles (SZAs) $< 75°$. The average deviations between our UV spectroradiometer and the world standard QASUME [55] have been shown to be <1%, i.e., well within the combined uncertainty of the two instruments.

On the other hand, the only instrument sensitive to wavelengths > 500 nm at the Aosta–Saint-Christophe observatory is a CMP-21 class-A pyranometer [33]. The instrument measures the downward short-wave irradiance integrated over the range of 300–3000 nm. Due to the narrower wavelength range covered by the AvaSpec compared to the pyranometer, the part of the solar spectrum missing from the former is compensated for by using a radiative transfer model, as described in Section 3.3. The pyranometer is calibrated every two years at PMOD/WRC. The calibration factor has an expanded uncertainty of 1.3% and has shown to be stable within 1% over 12 years.

The observatory also hosts sun-photometric devices to provide column amounts of atmospheric constituents. These were required as input to the radiative transfer model. In particular, a MkIV Brewer spectrophotometer was used to retrieve ozone [56,57] and nitrogen dioxide [58,59] vertical column densities, and a sun/sky POM-02 photometer was employed to estimate the aerosol optical depth (AOD) and microphysical/optical properties [60,61]. The aerosol properties were retrieved using the inversion algorithm Skyrad pack MRI (Meteorological Research Institute) version 2 [62].

2.2.3. Laboratory Equipment

Several light sources were employed to characterise the AvaSpec in the laboratory:

- Two 1000 W FEL lamps, calibrated at PMOD/WRC in the spectral range of 250–1200 nm (expanded uncertainty ranging from 5% at 250 nm to about 1% above 320 nm). These lamps are used on an optical bench after careful alignment with a laser and after measuring the distance from the lamp to the diffuser (since the diffuser is not flat, the optical reference plane, with respect to the external diffuser case, was determined at PMOD/WRC for a similar optic). The lamps are operated at a current of 8.1000 ± 0.0005 A, which is monitored through a feedback-loop controlled circuit based on a precision resistor and a voltmeter, both calibrated every year. The average difference between the Bentham responses obtained with different 1000 W lamps is usually within 0.1% in the 290–500 nm range. As the 1000 W lamps can only be used in the laboratory, and they should be turned on for as little time as possible (to preserve their calibration), our operating standards are 200 W lamps, described here below.
- A set of 200 W pre-aged quartz tungsten halogen (QTH) lamps. These are calibrated in the 250–500 nm range once a year with reference to the Bentham, after calibration of the Bentham itself with the 1000 W lamps. The 200 W lamps are operated at a fixed current of 6.300 ± 0.0005 A by a feedback-loop controlled circuit. Although they are less powerful than the 1000 W ones, they are employed in a portable field calibrator (PFC) fitting the input optic, where the distance between the lamp and the diffuser is about 25 cm. As a result, the irradiance from the 200 W lamps collected by the spectroradiometer is about twice as much as the one from the 1000 W lamps. The average deviations between the Bentham responses obtained from the different 200 W lamps of the available set are usually within 0.2–0.3%.
- A 4 W mercury vapour discharge lamp (USHIO), run on 0.3000 ± 0.0005 A. The well-known emission lines of mercury provide a useful reference for assessing the accuracy of the AvaSpec wavelength calibration.
- Two laser sources: a diode pumped solid state laser (DPSSL) emitting at 473 nm, in the blue region of the spectrum, and a simple red laser pointer with emission at 635 nm.

2.3. Measurement Periods

Three pilot campaigns were conducted to test the array spectroradiometer in the field. As this study was carried out in the frame of a brief internship (BSc of the first author), the instrument operated only for the following short measurement periods:

- Period 1 (P1): 23–24 August 2022;
- Period 2 (P2): 17–19 September 2022;
- Period 3 (P3): 4–7 January 2023.

The period of the year and the range of the available solar zenith angles varied widely among the three campaigns (Figure 1c), which allowed for testing of the spectroradiometer in quite different environmental conditions. The instrumental settings were also changed between P2 and P3, as explained in Section 4.3. Clear-sky days were preferentially selected for the comparisons, in order to avoid further complications related to the spectral synchronisation of the scans due to fast-moving clouds. Nevertheless, such cases were almost completely removed from the analysis thanks to the chosen measurement schedule (Section 3.2) and by accurately examining the spectral variability within the acquisition time. The aerosol amount was rather low during all campaigns, with maximum AODs of 0.1 at 500 nm in P2.

3. Methods

3.1. Characterisation and Corrections

As the characterisation of the AvaSpec and the signal corrections were a crucial part of this study, their general principles are thoroughly described in the following in the same order in which the corrections were applied to the data. Further details and quantitative results are provided in Section 4.1.

3.1.1. Dark Signal

Due to physical constraints, such as thermal sensitivity, all detectors employed in spectroradiometric systems show a small signal (noise and/or offset) even when they are not exposed to light [31,50,52,63]. In order to estimate the contribution of the dark signal without a shutter, we used two different techniques in combination. First of all, the dynamic dark correction, based on dedicated optical black ("blind") pixels, was turned on. In this way, even small changes due to temperature fluctuations or other effects were taken into account by subtracting a common baseline from all pixels. This correction, included in the firmware, was shown to improve the measurement accuracy on devices similar to ours [52,64]. Moreover, to account for the different behaviour of each pixel, we characterised the dark current spectrum (called "dark map") in the laboratory, as a function of the integration time. This was then subtracted from the dynamically corrected spectrum.

3.1.2. Non-Linearity

In an ideal instrument, the dark-corrected counts below the saturation threshold are proportional to the integration time and to the incoming irradiance. However, array instruments are heavily affected by non-linearity, which constitutes a major drawback in their use for solar irradiance measurements. Additionally, the bracketing technique is useless if linearity is not ensured. To correct for non-linearity, we examined the ratio between the dark-corrected signal and the integration time. To this purpose, we used a stable light source, represented by a 200 W lamp, and we measured its spectrum at different integration times. This typical ratio as a function of the counts defines the non-linearity error function. Since previous studies have mainly attributed the non-linearity effect to the ADC system as a function of the recorded counts [65], we do not consider it necessary to assess the non-linearity effects as a function of the light intensity.

3.1.3. Spectral Straylight

Spectral straylight is defined as light scattered inside the monochromator and detected by pixels not corresponding to the correct wavelength. This affects the shape of the recorded spectrum and has a particularly strong impact in regions with a steep spectral gradient, such as the UV-B range (280–315 nm) in solar measurements, thus making observations with array spectroradiometers very challenging for some applications. To estimate the straylight effect, it is necessary to observe the spectrum detected by the array corresponding to monochromatic emission (ideally, from a tunable laser). In the present study, we adopted a simple approach, previously described in the scientific literature [66], that only makes use of a few laser sources to build a deconvolution matrix [30,66]. In this way, the straylight was

numerically removed from both solar and lamp spectra by simple matrix multiplication. We also compared (Section 4.2) the technique described above with an even simpler approach based on the subtraction of a common straylight offset determined from wavelengths shorter than 290 nm and to the results when no straylight correction has been applied.

3.1.4. Diffuser Transmittance

The transmittance of polytetrafluoroethylene (PTFE) diffusers depends on temperature [51]. Although our diffusers are equipped with thermistors, extremely cold/hot weather, strong wind and precipitation may lead to temperature variations of some degrees. To compensate for this effect, we normalised the measured solar spectra using the Teflon transmittance functions available in the scientific literature [51].

3.1.5. Absolute Irradiance Calibration

Three methods to calibrate the spectral irradiance scale of the AvaSpec were compared:

- R1: response obtained in the laboratory from a 200 W lamp (250–500 nm);
- R2: response obtained in the laboratory from a 1000 W lamp (250–1200 nm);
- R3: response obtained in the field by transfer from the Bentham spectroradiometer (290–500 nm).

The customary traceability chain of a spectroradiometer usually involves calibration through lamps (e.g., in the laboratory), followed by independent comparison with a reference instrument (in the field). However, as shown by previous studies [67–69], incandescence lamps, such as those used in our current setup, are not the best way to calibrate the AvaSpec. Indeed, their emittance in the UV region is very low, and the sensitivity of the array spectroradiometer in the same range is also very weak; therefore, only low and noisy signals are expected. Moreover, the emission of incandescence lamps peaks in the infrared region (800–1000 nm), resulting in far-range straylight in the UV, which can be corrected only after a thorough straylight characterisation (or avoided via the use of cut-off filters or different light sources).

While this does not represent a problem for wavelengths $\gtrsim$ 500 nm, it greatly hinders accurate observations in the critical 290–500 nm range. Hence, we adopted a different, more pragmatic approach aiming at focussing on the best possible performances achievable by the AvaSpec:

- For wavelengths $<$ 500 nm, the AvaSpec response was determined by transfer (R3 in the above list) from the Bentham. This was obtained as an average from only a small subset of the spectra (SZA $< 40^{\circ}$, collected on 23 August 2022, during P1);
- While the AvaSpec and the Bentham were no longer independent in a strict sense, comparison over a long period (P1–P3) and a wide range of solar angles, and, therefore, of very different shapes and intensities of the solar spectrum, provided clear information about the reliability and stability of the R3 response;
- We compared R3 with the responses obtained from the lamps (R1–R2);
- We demonstrated that in the critical range of 290–500 nm, in which absolute calibration is challenging, the lamps can at least be used in a relative sense, i.e., to check the stability of the instrument and track its spectral variations (Section 4.2);
- Possible improvements to our calibration setup in the future are discussed in Section 5.

For wavelengths $>$ 500 nm, the response obtained with a calibrated 1000 W lamp was used, as in the conventional approach.

3.1.6. Wavelength Alignment

An accurate alignment is especially important in regions of the solar spectrum with strong gradients, as small wavelength shifts can trigger large errors in the measured irradiance. The wavelength alignment was accomplished here in two steps. First, the dispersion function (the pixel–wavelength relationship) provided by the manufacturer was checked at particular wavelengths using well-known emissions lines from a mercury lamp

(Section 2.2.3). This characterisation was carried out in the laboratory at the beginning of P1 and P3 and resulted in a significant average offset, which was subtracted from all spectra. Second, for an even better alignment, we processed the spectra (in the wavelength range of 290–600 nm) with the SHICrivm software (version 3.096, compiled on GNU/Linux) [70]. The algorithm allows for corrections accurate to ±0.02 nm based on the correlation with the fine structure (Fraunhofer lines) of the solar spectrum. The software also allowed us to standardise the measurements from both the AvaSpec and the Bentham with a triangular, 1 nm wide (FWHM) bandpass function and to interpolate them (with a physically based technique) to a common and regular wavelength grid for a consistent comparison. Although more advanced algorithms have been developed recently [55], which also take into account the variable resolution of the array spectroradiometer with the wavelength, the latter has not been characterised so far, and the SHICrivm software was considered sufficient for the purposes of the present study.

3.1.7. Integrated Quantities

The spectra measured by the AvaSpec can be integrated on different wavelength ranges to obtain broadband quantities. One of these is the global solar UV index, defined as:

$$\mathrm{UVI} = \frac{\int_{290\,\mathrm{nm}}^{400\,\mathrm{nm}} I(\lambda)\, E(\lambda)\, d\lambda}{C} \tag{1}$$

where $I(\lambda)$ is the spectral solar irradiance (expressed in W m^{-2}), e.g., from the AvaSpec, and $E(\lambda)$ is the erythemal action spectrum [71], while the denominator $C = 25$ mW m^{-2} is an empirical normalisation factor for providing indices approximately between 1 and 10. The UV index has become a global standard aimed at the general public for communicating the effectiveness of UV radiation in producing sunburn and other derived health issues.

We also define the global horizontal irradiance (GHI) as the total power per unit area of the short-wave solar radiation reaching the ground as:

$$\mathrm{GHI} = \int_{290\,\mathrm{nm}}^{3000\,\mathrm{nm}} I(\lambda)\, d\lambda \tag{2}$$

where the limits of the integral encompass almost all of the total solar irradiance.

3.2. Measurement Schedule and Synchronisation with Reference Instruments

All instruments employed in this study were synchronised through the network time protocol (NTP). Nonetheless, further efforts were required to compare the solar spectra collected almost instantaneously by the AvaSpec and those scanned during an interval of 5 min by the Bentham spectroradiometer. Moreover, measurements at different integration times had to be recorded by the AvaSpec to allow for bracketing. We proceeded as follows:

1. An AvaSpec measurement sequence included bracketed acquisitions at three integration times: 1000, 100 and 10 ms. A total sampling time of 5 s was set for each exposure, leading to 5, 50 and 500 samples for each integration time, respectively (average and standard deviation were calculated from the ensemble). These settings were estimated to be suitable for accurate measurements both in spectral regions where solar irradiance and the detector efficiency are low (UV and IR) and where they are large (visible range). The sequence above was repeated in reverse order, which allowed: (a) minimisation of the bias due to linear changes of solar irradiance within the acquisition time; (b) careful control (and filtering) of fast-moving clouds, which would have limited the accuracy of the comparison with the Bentham; (c) calculation of an effective timestamp for the measurement (as the middle time of the six resulting spectra).
2. The previous sequence was repeated for the whole duration of the Bentham scan (about 5 min) to allow for subsequent wavelength-to-wavelength comparison with the

Bentham. The overall procedure was restarted every 15 min, which is the repetition period of the Bentham.

3. A matrix of the AvaSpec spectra acquired during a Bentham scan was built. Since the timestamp when the Bentham is scanning a specific wavelength is recorded, the nearest neighbour interpolation with the proper element of the AvaSpec matrix allowed us to simulate a scan-like spectrum from the AvaSpec for comparison with the Bentham.

The previous steps were not needed when using data from broadband instruments (e.g., pyranometer), the measurements of which are also instantaneous. Hence, in these cases, all data from the AvaSpec acquisitions were retained and associated with the broadband series by simple time interpolation.

3.3. Radiative Transfer Model

Simulations with the libRadtran radiative transfer model [72] version 2.0.4 were performed both for comparison purposes, as in previous studies [16,68,73], and to correct the AvaSpec measurements for the unmeasured part of the spectrum when calculating the global horizontal irradiance (Section 2.2.2). This aim was achieved by deriving the following factor:

$$f = \frac{\int_{290\,\mathrm{nm}}^{3000\,\mathrm{nm}} I(\lambda)\,d\lambda}{\int_{290\,\mathrm{nm}}^{1100\,\mathrm{nm}} I(\lambda)\,d\lambda} \tag{3}$$

where I is the spectral irradiance from the model, and the integration limits are representative of the CMP-21 pyranometer and the AvaSpec, respectively.

The model was configured as in Table 1, with most parts of the input coming from the ancillary instrumentation at the observatory. Although retrievals of precipitable water vapour are possible with the POM-02 photometer and were performed at Aosta–Saint-Christophe in the past [74], they are not yet an operational product. Hence, the amount of water vapour leading to the best agreement between the observed spectra and the simulations was chosen as the input to the model.

Table 1. Configuration of the radiative transfer model.

Parameter	Reference/Source
Solver	DISORT
Band parametrisation	REPTRAN (fine)
Extraterrestrial spectrum	TSIS-1 [75]
Atmosphere	Standard midlatitude summer/winter [76]
Ozone cross-sections	Bass & Paur [77]
Ozone vertical column	Brewer spectrophotometer
Nitrogen dioxide vertical column	Brewer spectrophotometer
Aerosol optical depth and properties	POM-02 photometer
Water vapour	Determined based on best fit with AvaSpec measurements

4. Results

Since the present manuscript may act as a reference for future studies with our AvaSpec, the results of the laboratory characterisation are reported in detail (Section 4.1). Subsequently, the results of the first tests in the field are discussed with reference to specific spectral ranges: the 290–500 nm (Section 4.2) range and integrated short-wave (Section 4.5). Some considerations about the instrumental stability (Section 4.3) and results from the radiative transfer models (Section 4.4) are also included, as they are both important topics for the assessment of the short-wave integrated irradiance.

4.1. Initial Laboratory Characterisation

First of all, the dark current was characterised for each pixel as a function of different integration times, ranging from 2 ms to 50 s. A residual structure is clearly visible in

the dark spectra even with the dynamic dark correction turned on (some examples are provided in Figure S1), showing that this fine characterisation is fundamental, especially at long integration times.

Secondly, non-linearity in the AvaSpec was determined from the emission spectrum of a 200 W lamp recorded at 30 different integration times, ranging from 10 to 700 ms. The count rates, i.e., the ratio between the (dark-corrected) counts and the integration time, were then calculated. Their variation as a function of the counts was normalised to the ratio corresponding to 40,000 counts for each pixel. The results are presented in Figure 4a, where it can be noticed that the instrument underestimates the count rates by about 6% in low-light conditions or, even more, at the saturation limit. The error due to non-linearity was parametrised with a locally estimated scatterplot smoothing (LOESS) interpolation, the inverse of which represents the correction that we must apply to the signal. This same training data set was then employed to check the efficiency of the correction. After correcting, the residuals to the fit were within ±0.5% (Figure 4b). The test also revealed (Figure S2) that the instrument is not affected by any blooming effect, i.e., measurements at pixels close to those exposed to saturation are still correct. As a consequence, it is possible to safely use the bracketing technique and saturate part of the signal to increase the dynamic range of the instrument.

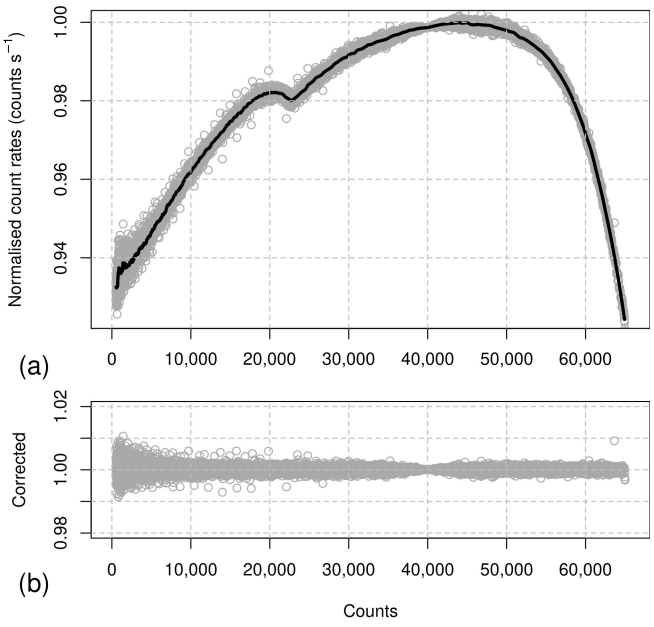

Figure 4. Effect of non-linearity in the AvaSpec. (**a**) Ratio between count rates (as a function of the counts) and the same quantity measured at 40,000 counts. The results were further normalised to the maximum of the curve. The thick line is a locally estimated scatterplot smoothing (LOESS) interpolation through all points (grey). (**b**) Same as (**a**) after non-linearity correction.

As a third step, the two laser spectra needed to determine the straylight correction matrix were measured (Figure 5). In order to accurately characterise the whole line-spread function (LSF), i.e., both the peak and the tail (about five orders of magnitude lower), the spectra were acquired with different integration times (from 2 ms to 10 s). Composite spectra, one for each laser, were then obtained after non-linearity correction. The corresponding LSFs were aligned to a common wavelength scale and then scaled to best match their tails. The region close to the red laser peak (±50 nm) was removed due to double diffraction, a phenomenon also found by other groups [30]. The two scans were merged and scaled to the integral of the in-band region (from the blue laser). The signal in this region was then set to zero to only retain the effect of straylight (and not of the finite resolution). The in-band region was arbitrarily defined as the area within ±10 nm of the peak. Although this interval is much larger than the spectral resolution, it was chosen for

reasons of numerical stability in the inversion of the straylight matrix (condition number), as mentioned in other studies [31]. The two tails were fitted independently with a smooth exponential function of the wavelength ($y = c + b\lambda^{-a}$, similarly to [66]). As also pointed out by Kreuter and colleagues [66], an accurate determination of the offset c is particularly challenging. Instead of using optical filters, as in previous works, we determined the offset by minimising the differences between the responses obtained from the lamps (R1 and R2 as in Section 3.1.5) and the response transferred from the Bentham (R3). The final function is plotted together with the laser spectra in Figure 5.

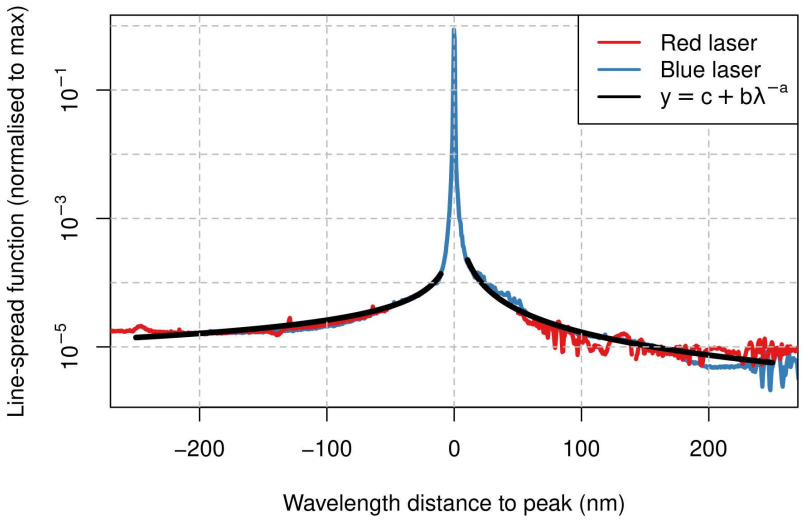

Figure 5. Line-spread function from the red and blue lasers recorded by the array spectrometer. The region close to the red laser peak (±50 nm) was removed due to a double diffraction. Each tail was fitted independently using the formula in the legend.

The AvaSpec response was determined in the laboratory using two pairs of sources: two 1000 W FEL lamps (F694 and F698) and two QTH 200 W lamps (KS147 and KS148). The relative deviations of the AvaSpec response obtained with each lamp pair to their respective average are shown in Figure S3. It is interesting to notice that the 1000 W setup looks slightly more stable than the 200 W one; however, the responses obtained by each pair of lamps generally agree within ±0.5%. As can be seen in the figure, noise prevails at the shortest wavelengths despite the long integration times, up to 10 s, since both the lamp emission and the detector sensitivity are very low in this spectral range. A comparison of these results with the response obtained by the transfer from the Bentham is provided in Section 4.2.

Finally, to check the dispersion function, we considered the most intense emission lines from the mercury lamp, and we associated their wavelengths with the pixels corresponding to the measured peaks. Since the wavelength step of the instrument is only slightly narrower than the spectral resolution, each line is detected by only a few pixels, and interpolation with an analytical function (here, a Gaussian) is needed to properly define the peak. Double mercury lines within the instrumental resolution were carefully excluded from the analysis. Figure S4 shows the wavelength misalignment from both the mercury test, at selected wavelengths, and from the output of the SHICrivm program, over the whole 290–600 nm range. The two methods consistently revealed an overall misalignment of about 2.5 nm in period P1, which increased to 3.7 nm in period P3 in different ambient conditions (box temperature). This highlights the need to accurately characterise the instrument in the conditions under which it is actually operated. The previously described Gaussian fits also provided the bandwidth of the instrument, corresponding to about 0.9 nm FWHM, which is in good agreement with the specifications of the manufacturer. The available data did not allow us to infer any dependence of the resolution on the wavelength. Hence, we

employed all measured emission lines, aligned with respect to the wavelength distance from their respective peak, to obtain the AvaSpec slit function (Figure S5). The latter was fitted, in turn, with a Gaussian for later use with SHICrivm.

4.2. Preliminary Test in the Field–UV-Visible Range (290–500 nm)

For the sake of simplicity, we first focus on a single, clear-sky day (23 August, P1). Measurements on other days and periods will be described afterwards. Figure 6 shows the daily evolution of the UV index (Section 3.1.7), processed with different straylight correction algorithms (Section 3.1.3). While the results without any straylight correction are meaningless for most applications, the UV index obtained by subtracting a constant offset (from wavelengths < 290 nm) approximates the Bentham measurements more accurately for solar zenith angles $\lesssim 50°$. The straylight matrix correction, however, outperforms the previous methods and leads to an agreement of better than about $\pm 5\%$ between the AvaSpec and the Bentham for SZAs $\lesssim 70°$. Although the calibration was transferred from the Bentham to the AvaSpec on the same day (from measurements at an SZA $< 40°$), the results indicate that such a response works well even when the sun is much lower on the horizon. Moreover, the good AvaSpec performances over a wide range of UV indices demonstrate that the non-linearity effects are adequately compensated (Section 3.1.2).

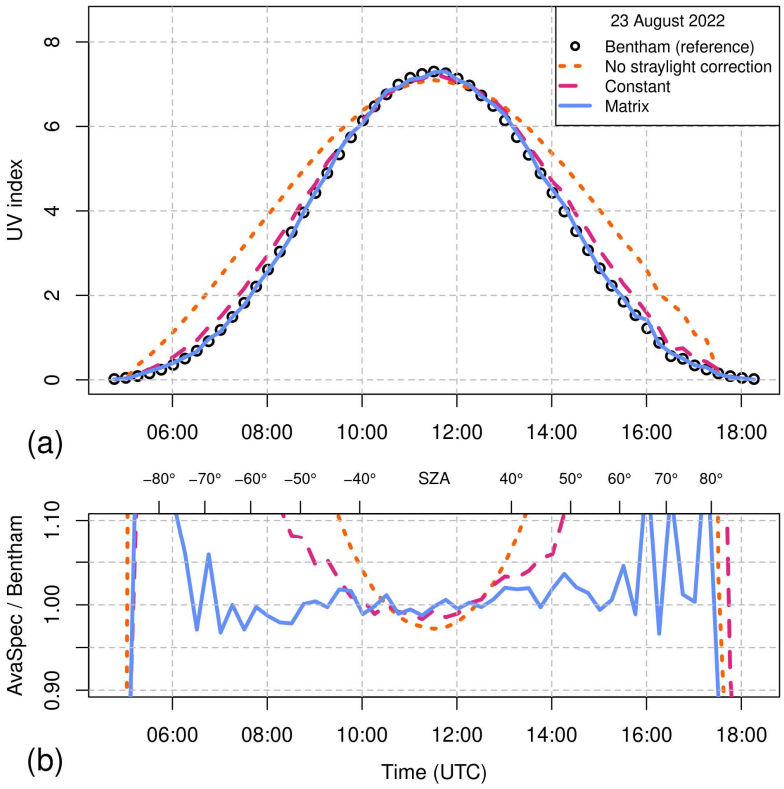

Figure 6. (**a**) Evolution of the UV index on 23 August 2022 (P1). The three coloured lines correspond to the AvaSpec measurements with three straylight corrections, while the dots represent the UV index from the Bentham (reference). (**b**) Ratio between the UV index from the AvaSpec and from the Bentham, as a function of time of the day and solar zenith angle (SZA, upper axis; negative values referring to morning, positive to afternoon).

The ratio between the spectral irradiance by both instruments is shown in Figure 7a as a function of the solar zenith angle for a selection of wavelengths and, in Figure 7b, for the whole 290–500 nm range. The ratio is generally between 0.95 and 1 in the wavelength range of 315–500 nm and for SZAs $< 70°$ with an average deviation of -1.5%. The agreement is comparable to that obtained by instruments specially designed for UV-visible measurements. At shorter wavelengths, noise overcomes the signal, as already noticed

(Section 4.1). Additionally, at longer wavelengths (450–500 nm) and SZAs $> 70^\circ$ the agreement worsens, with deviations as large as -10% at SZA$= 80^\circ$ in the morning (-5% at the same SZA in the evening). This behaviour, as a function of the solar zenith angle and wavelength (Figure 7a), may be evidence of an imperfect angular (cosine) response, as the direct component of the solar irradiance becomes dominant at longer wavelengths. A possible hint to support this hypothesis is the fact that the variability seems to decrease in overcast sky conditions (which have been excluded from the analysis due to increased noise). Although the optics of the AvaSpec and the Bentham should be identical, slight differences may occur as a result of manufacturing processes or coupling with different fibre optics. The effect of inaccurate corrections, such as straylight, cannot be the cause of the observed behaviour owing to the fact that the zenith dependence occurs at wavelengths where the straylight effect is minimum, and the count rates are in their best measurement range. Additionally, an azimuthal dependence (approximately in the northwest direction) could be the reason for the slight asymmetry between morning and afternoon. This second effect was confirmed by examining the ratio of the AvaSpec and the Bentham before/after turning the AvaSpec optic 180° (Figure S6).

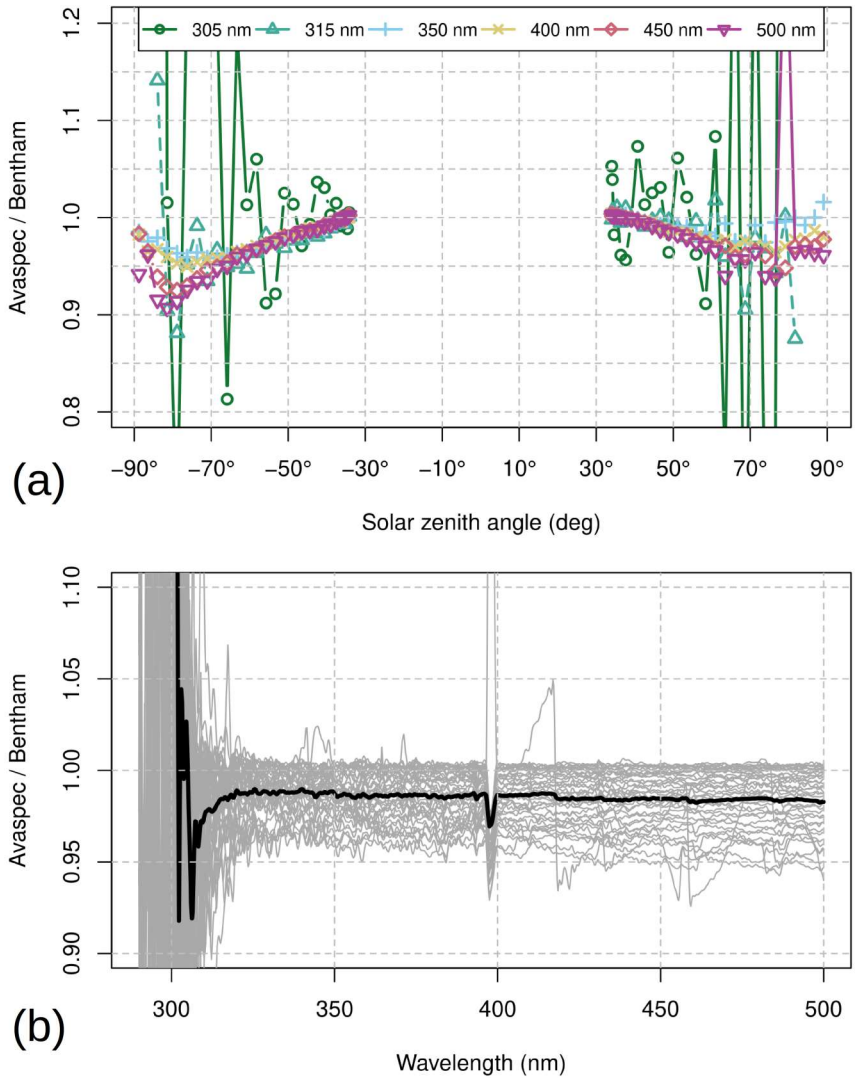

Figure 7. Comparison of the spectra measured on 23 August 2022 by the Avaspec and the Bentham (reference) spectroradiometers. (**a**) Ratio at specific wavelengths as a function of the solar zenith angle (negative values refer to morning, positive to afternoon). (**b**) Ratio of all spectra at SZAs $< 70^\circ$ (grey lines) and their average (bold line), as a function of wavelength. The dip at about 400 nm is due to two Fraunhofer lines in the solar spectrum, which were not fully compensated for by SHICrivm.

The agreement between the AvaSpec response determined from the 200 W and 1000 W lamps, with respect to the one obtained by transfer from the Bentham (in P1), is depicted in Figure S7. While most of the data lie in the interval ±10%, some deviations can be seen around 400 nm, close to two deep Fraunhofer lines in the solar spectrum (Calcium-II doublet). Small residual shifts or imperfect normalisation of the bandpass by the SHICrivm algorithm, perhaps due to slight variations in the slit function with wavelength, could be the reason for the observed behaviour. Additionally, the comparison shows that noise increases for wavelengths $\lesssim$ 315 nm due to the low emission of the lamps in the UV, which was previously described as a main limitation of using such lamps for calibrating the instrument.

The whole data set P1–P3 is presented in Figure 8. Since these data were processed using the initial calibration (23 August 2023), the instrument can be considered very stable, in the erythemal range, over several months. Indeed, the daily median ratios between the AvaSpec and the Bentham in P1 and P2, and their interquartile distances, lie in the ±5% range. The relative deviations in P3 increase; however, it must be noted that UV irradiances are very low in January (even lower than the threshold used in the non-linearity correction), the solar zenith angles are always $\gtrsim$68° and the sun is below the mountains for most parts of the day (Figure 1c). In fact, the absolute deviations between the two spectroradiometers in P3 are negligible, of the order of 0.1 UV indices.

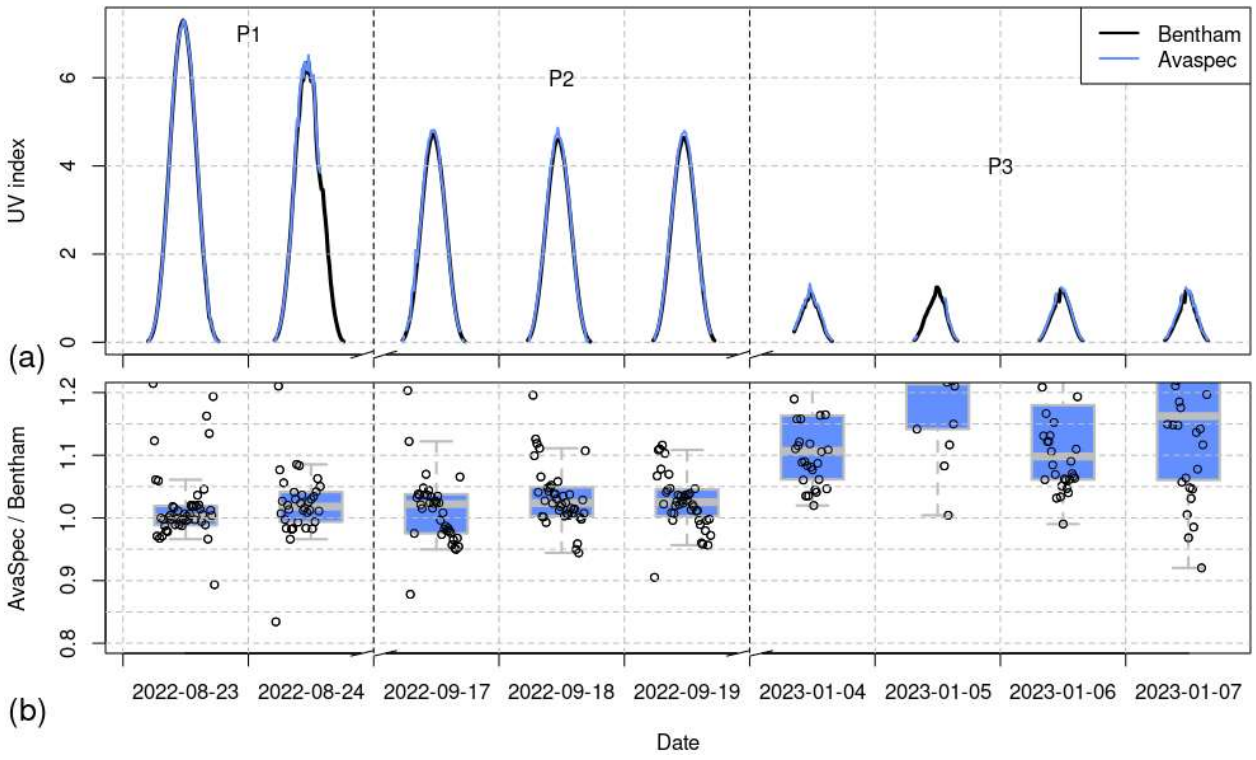

Figure 8. (**a**) UV index measured by the Bentham (reference) and the AvaSpec during the three intensive periods. All data were processed using the response determined on 23 August 2022. (**b**) Ratio between the UV index measured by the AvaSpec and the Bentham. Notice that: (1) all data are plotted (circles), even those collected at very large SZAs (morning/evening and winter) or with the sun behind the mountains; (2) some days have incomplete measurements (e.g., 24 August, 5 January), which could hinder the comparison. The coloured area of the boxplots in the background indicates the interquartile distance (25–75%), while the baffles represent the whole range of the data with the exception of the outliers.

At wavelengths in the range of 315–500 nm, the response of the AvaSpec is stable from P1 to P2, and the spectral ratios with the Bentham are within the range from −5 to 0% (not shown). However, the response at these wavelengths changes sharply in P3. The variations

in the instrumental responsivity between P1 and P3, based on a comparison of the count rates from the 200 W and 1000 W lamps, are about −5% for wavelengths < 315 nm, but they gradually worsen in the range 400–900 nm (Figure S8). Although some research groups reported rapid variations of the spectroradiometer response in the first months of usage [73], these changes are much larger than those generally expected from typical detectors used in array spectroradiometers [68] and inevitably raise some doubts about the quality of the AvaSpec measurements. However, this may be a contingency linked to the different settings of the operating temperature in the two periods or to the extensive tests performed on the instrument (next Section 4.3) and likely changing its sensitivity. Thankfully, although we showed that the lamps cannot be used for absolute calibrations in the present configuration, they can be employed, in a relative sense, to track changes in the AvaSpec response. Figure 9 depicts the ratio between the AvaSpec response determined in three different ways with respect to the response transferred from the Bentham in P3. As mentioned before, using the response calculated in P1 for P3 triggers errors larger than 30%, owing to the change in the radiometric sensitivity and the additional cosine/azimuthal dependences of the optic (the solar zenith angle increases greatly from P1 to P3). The AvaSpec response determined directly from the 200 W lamp would reduce the errors on average; however, it presents spectral shapes similar to those in Figure S7. If we use the ratio of the measurements from the same 200 W lamp in P1 and P3 as a proxy of the changes in the sensitivity of the AvaSpec, then we obtain a rather flat ratio for the transferred response, which likely depends on the residual effect of the input optic. Despite the limited amount of collected data, we believe that this result demonstrates the possibility of checking and correcting the AvaSpec response in the long term (e.g., months) based on 200 W lamps.

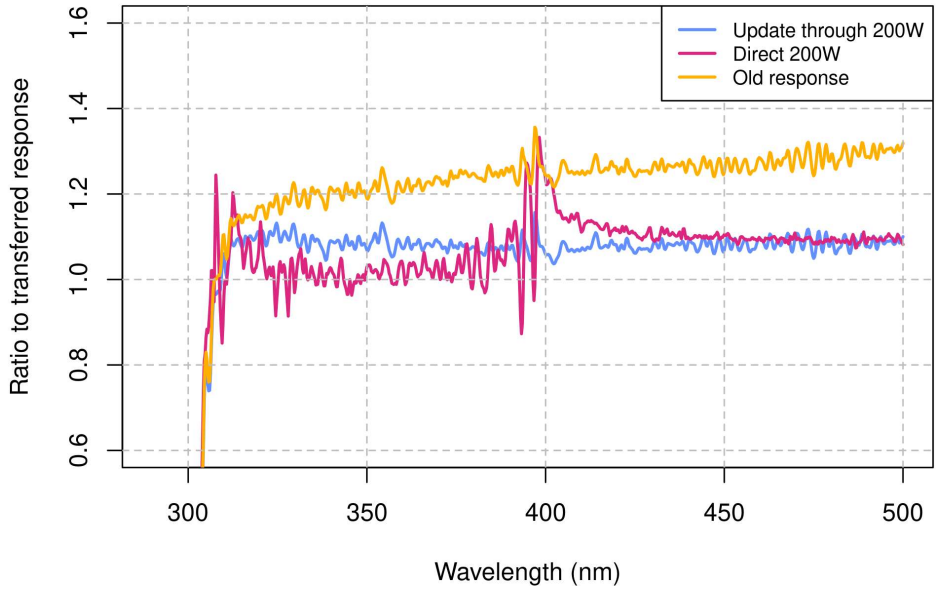

Figure 9. Ratio between the AvaSpec response determined in three different ways with respect to the reference response (transferred from the Bentham in P3): response calculated in P1 (yellow, "old response"); response determined directly from the 200 W lamp (pink line); response transferred from Bentham in P1, further updated based on changes of the lamp measurements between P1 and P3 (blue line).

4.3. Stability Issues

As mentioned in Section 4.1, the spectral response of the AvaSpec obtained with the 1000 W lamps shows some spectral structures in the 700–900 nm wavelength range. These structures are not reported in the lamp certificate and are also visible in the raw (uncalibrated count rates) solar spectra, hence, they depend on the AvaSpec. Moreover, some signs of exacerbation were seen in P2 (not shown). Even on shorter time scales (day-to-day), the spectral structures were unstable, so they could not be removed from the

irradiance spectra by the absolute calibration, and they clearly emerge in the comparison with the radiative transfer model (Section 4.4). Another symptom presumably connected to this behaviour is that the integrated irradiance in the short-wave range (Section 4.5) seems less stable from P1 to P2 than the UV-visible irradiance (Section 4.2).

The most likely explanation is that water vapour condensation occurred over the detector as a result of the large temperature difference between the temperature in the box and the temperature of the detector (set to 5 °C) and moisture leakages in the monochromator. Indeed, the dew point temperature was higher than the detector temperature even for the rather dry atmospheric conditions outside the laboratory. Similar issues related to condensation were reported in previous studies [50,73]. Therefore, some actions were taken between P2 and P3 to mitigate the problem:

- The AvaSpec was kept for some time in a very dry place, together with silica gel desiccant;
- Meanwhile, desiccant bags were also put in the temperature-stabilised box and regularly changed since placement;
- When the AvaSpec was reinstalled in the temperature-stabilised box, thermoelectric cooling (TEC) was temporarily deactivated for some days to ensure as much drying as possible;
- The temperature in the box was decreased to avoid too large of a temperature jump with respect to the detector.

It must be noticed that the detector temperature must not be increased, as the dark current is extremely sensitive to this parameter.

The previous operations, including the characterisation of the instrument at a different TEC temperature, long periods of inactivity and configuration changes had impacts on the AvaSpec sensitivity, which decreased from P2 to P3. As a positive effect, while some spectral structures remain in the responsivity in P3, their amount and variability appear to be reduced. Repeated measurements of the AvaSpec response, even after exposure to the sun, during P3 (from 7 December 2022 to 19 January 2023) show maximum variations of well within 1% (Figure S9).

4.4. Comparison with a Radiative Transfer Model

The spectral irradiance measured by the AvaSpec was compared to that of libRadtran. Radiative transfer models are useful to check the proper functioning of the system, especially if no other reference instrument is available for spectral comparison, as in our case for the range not scanned by the Bentham. A good comparison between the measurement and model also justified the use of the latter for extending the irradiance spectrum beyond 1100 nm.

Figure 10 presents two examples, taken from P1 and P3, respectively. In the first case, the agreement between the measured and simulated spectra is very good (within ±5%) over the whole AvaSpec wavelength range; however, a critical region with some lines is visible in the range of 700–900 nm (mentioned above, Section 4.3). In the second case, these lines are no longer visible, as the instrument during P3 is very stable, and the absolute calibration procedure compensates for this effect. However, an average offset of −10% can be distinguished, likely due to the optic, as mentioned in Section 4.2. It should be also noticed that the solar irradiance in P3 is extremely low; hence, relative ratios should be taken with caution.

Finally, the compensation factor needed to compare the AvaSpec with the pyranometer was calculated with libRadtran as in Equation (3). This factor was found to be a smooth function of the solar zenith angle and not sensitive to the accurate aerosol amount/properties in the pristine conditions encountered during the three periods. For P1 and P2, the factor was $f = 1.22$, while, for P3, it was 1.25 due to the lower precipitable water vapour in winter.

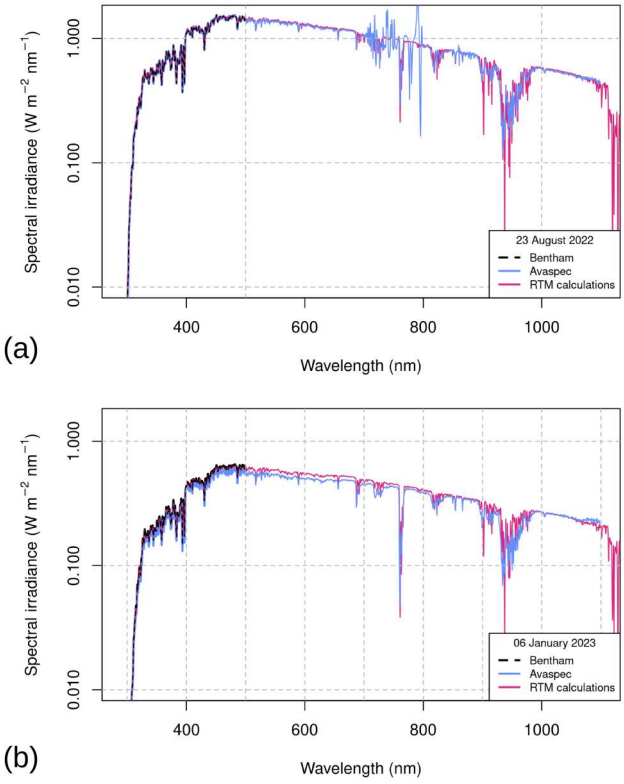

Figure 10. Comparison of the spectral irradiance measured by the Bentham (dashed black line) and by the Avaspec (blue line) with the output of the radiative transfer model (pink line): (**a**) 23 August 2022 (11:30 UTC). The calibration used here in the 290–500 nm range for the AvaSpec was obtained by transfer from the Bentham, while irradiance in the range of 500–1100 nm is based on calibration with a 1000 W lamp; (**b**) 6 January 2023 (12 UTC). Irradiance in the 290–500 nm range was obtained by updating the response transferred in P1 based on measurements from a 200 W lamp in P1 and P3.

4.5. Preliminary Test in the Field–Integrated Short-Wave Irradiance

As performed in Section 4.2 for the 290–500 nm range, we start by considering one single day (23 August 2022) to illustrate the comparison between the global horizontal irradiance measured by the AvaSpec and the CMP-21 pyranometer. Figure 11 shows that the integral of the spectral irradiance in the measurement range of the AvaSpec is lower than the one detected by the pyranometer. However, if the proper compensation factor f is applied (Section 4.4), the estimates by the two instruments are reduced to $\pm 5\%$ up to 80° SZA (some cirrus clouds perturb the comparison at the end of the afternoon). The results are very promising, especially considering that measurements by the AvaSpec and the CMP-21 in the considered wavelength range are independent (as opposed to those in Section 4.2).

The whole short-wave data set is presented in Figure 12 and compared with the pyranometer. The data in periods P1 and P2 employ the 1000 W calibration from P1. Unfortunately, we did not calibrate the AvaSpec in P2; hence, the decrease in its responsivity (already discussed in Section 4.3) could not be compensated for. Lamp measurements were again performed in P3. Therefore, as we have already tested for UV-visible measurements, we employed the ratio of the irradiance emitted from a 200 W lamp in P1 and P3 to update the initial response determined with a 1000 W lamp in P1. The results were additionally compared to those obtained in P3 via direct 1000 W calibration (<1%, not shown). The good agreement between the AvaSpec and the CMP-21 in P3, visible in Figure 12, demonstrates that is it possible to use the 200 W portable calibrator, instead of our primary standards (1000 W lamps), to track sensitivity variations in the visible and near-IR regions, thus avoiding frequent and complex calibrations in the optical laboratory.

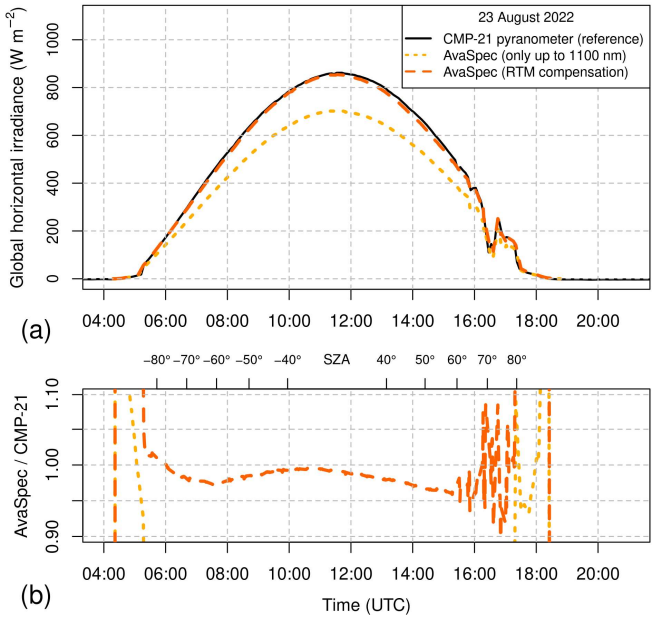

Figure 11. (**a**) Evolution of the global horizontal irradiance on 23 August 2022 (P1). The lines correspond to measurements from the CMP-21 pyranometer (black) as well as spectra from the AvaSpec integrated only up to 1100 nm (yellow, dotted line) and from the AvaSpec after RTM compensation for the unmeasured part of the spectrum (orange, dashed line). (**b**) Ratio between the GHI from the AvaSpec and from the CMP-21 pyranometer, as a function of time of the day and solar zenith angle (SZA, upper axis; negative values referring to morning, positive to afternoon). Cirrus clouds perturb the measurements in the late afternoon.

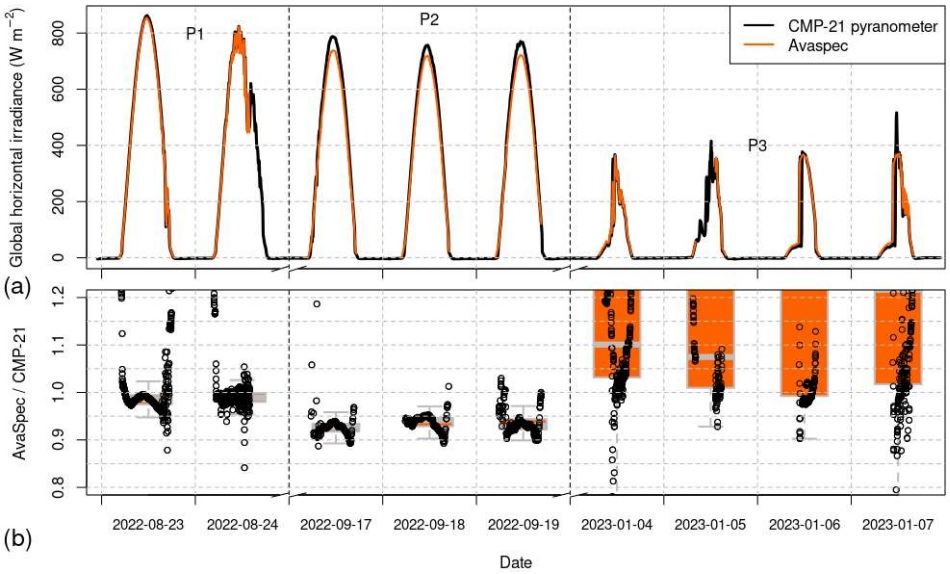

Figure 12. (**a**) Global horizontal integrated irradiance measured by the CMP-21 pyranometer (reference) and the AvaSpec (after compensation for the missing part of the spectrum) during the three intensive periods. (**b**) Ratio of the global horizontal irradiance measured by the AvaSpec and the CMP-21. Notice that data in P2 use the outdated calibration from P1. The coloured area of the boxplots in the background indicates the interquartile distance (25–75%), while the baffles represent the whole range of the data (circles) with the exception of the outliers.

5. Discussion

The first results from the AvaSpec derived in the previous sections are comparable to those reported in the existing scientific literature, especially from instruments not specifically designed/customised for a given spectral range (see Table S1 for the comparative analysis).

In this first study, we tried to assess the best possible performances of the AvaSpec by transferring the response from a reference instrument and partly bypassing the difficulties in calibrating the instrument with our current setup in the 290–500 nm range. Similar methods were employed in previous studies [49,78]. Indeed, as discussed in Section 3.1.5, the use of incandescence lamps to calibrate array spectroradiometers in regions of weak sensitivity, such as UV and IR [68,69], is problematic with our current system. The latter can certainly be improved in the future, e.g., by employing optical cut-off filters [16,48,67], and thus reducing the infrared component of the irradiance, or even by using completely different light sources, such as LEDs [79] (stability requirements in absolute calibrations would exclude deuterium lamps from the choice [22]). However, we also demonstrated that the response can be determined by transfer once for all (or with a rather low frequency), and then tracked this through the use of 200 W lamps in a relative way. We will adopt this solution until new calibration methods are explored at the observatory.

Two other issues affect our AvaSpec: the imperfect angular response of the optic and the presence of spectral structures in the 700–900 nm range. With regards to the first point, measurements in a more equipped optical laboratory will allow us to characterise the angular response and correct for it using a modelling approach. However, the issue is expected to manifest itself only at high solar zenith angles, such as in the early morning, late afternoon and winter, thus affecting only low solar irradiances. As for the second point, although the observed spectral features did not disappear, the instrument was very stable in the last period, and the absolute calibration, therefore, can be employed to fully compensate for this effect. Unfortunately, this specific kind of spectrometer does not lend itself to a repair, since the AvaSpec model is closed with a kit, making it impossible to open the instrument without damaging it beyond repair (T. van den Broek, Avantes, personal communication). The newer model that has replaced this one, however, does not have this issue and can be repaired. More generally, the used Avantes material is from 2017, while improvements to their products have been made that may positively influence results.

As a final remark, this preliminary work does not treat the uncertainty of the AvaSpec. Indeed, we believe that a large part of the uncertainty is contributed by long-term instability, and, to date, we have not collected enough data to characterise the latter. Regardless, we do not expect the uncertainty to be very different from the one determined in previous studies with other array instruments, e.g., [31,80].

6. Conclusions

A commercially available AvaSpec ULS2048-LTEC array spectroradiometer was tested for the first time at the Aosta–Saint-Christophe solar observatory. The results of the characterisation and from three pilot campaigns conducted in different periods of the year provide the following answers to the scientific questions driving the research (see Introduction).

1. Can a single array spectroradiometer make reliable measurements of global irradiance in a wide spectral range, encompassing UV, visible and near-IR wavelengths simultaneously?

   The preliminary results show that the AvaSpec is able to measure the spectral irradiance in the 290–500 nm interval and the UV index with an accuracy of $\pm 5\%$ for solar zenith angles $< 70^\circ$ ($\pm 10\%$ at SZA = 80°) if the absolute calibration is transferred from the reference spectroradiometer from a small subset of measurements. Then, 200 W and 1000 W incandescence lamps can be employed, in a relative sense, to track the long-term spectral responsivity changes of the Avaspec and compensate for them. The comparison of the AvaSpec irradiance integrated over the short-wave solar range and

that from a co-located CMP-21 pyranometer (approximately 300–3000 nm) resulted in consistency with an agreement between these two instruments within ±5%.

2. What minimal procedures are required to characterise and calibrate the AvaSpec and obtain measurements of satisfactory quality?

   The initial characterisation in an optical laboratory was crucial for investigating some instrumental features and artefacts of the instrument and to collect the data needed for the radiometric corrections to be applied when the instrument is operated in the field. As a minimum requirement, we recommend characterisation of the dark signal, non-linearity, spectral straylight and wavelength shifts. Notably, spectral straylight must be taken into account through the use of a correction matrix if measurements in the UV range are expected.

3. How good is the agreement between the AvaSpec measurements and the radiative transfer model (RTM) simulations?

   The spectral irradiance in the whole AvaSpec measurement range (290–1100 nm) agreed within ±5–10% with the output of a radiative transfer model, when the ancillary measurements from co-located instruments were given as input to the RTM.

4. What are the strengths of the new system compared to the existing reference instruments?

   Array spectroradiometers are compact and portable, and their cost is about one order of magnitude lower than that of reference scanning instruments. Based on our experience, the main advantage of array systems with respect to more traditional instruments is their wide spectral range, covering most parts of the solar short-wave region. The measurement speed may also be a significant advantage of array spectroradiometers; however, the use of the bracketing technique to optimise the signal-to-noise ratio (depending on the spectral range of interest) may decrease the measurement frequency.

The results presented here are the first ones obtained from this kind of instrument at the Aosta–Saint-Christophe observatory. The data from the AvaSpec will be useful, for example, in the agency research programs that are focussed on renewable energy production. Another step is the application of the expertise gained during this study to set up a similar array spectrometer in a direct-sun configuration, using a solar tracker. This will allow us to strengthen the current research activities on the topic of solar spectrophotometry for monitoring atmospheric composition.

Supplementary Materials: The following supporting information can be downloaded at: https://www.mdpi.com/article/10.3390/en16072998/s1, Table S1: Non-exhaustive list of previous studies involving array spectroradiometers; Figure S1: Example of the dark current spectral structure after application of the dynamic correction; Figure S2: Count rates measured by the AvaSpec from a 200 W lamp, at two different integration times; Figure S3: Ratio between AvaSpec responses determined with the two lamp sets relative to their respective averages; Figure S4: Wavelength misalignment of the AvaSpec as determined from the mercury lamp test and from the SHICrivm algorithm; Figure S5: Instrumental bandpass; Figure S6: Azimuthal dependences of the AvaSpec and Bentham optics; Figure S7: Spectral ratio between the AvaSpec response obtained with the calibration lamps and by transfer from the Bentham spectroradiometer; Figure S8: Ratio between the AvaSpec responses measured on 19 January 2023 and 16 August 2022; Figure S9: Ratio between the AvaSpec responses measured on 19 January 2023 and 7 December 2022. The supplement includes the following references [3,7,11,16,23,28,29,48,66–69,73,81–94].

Author Contributions: Conceptualization, O.P. and H.D.; Formal analysis, O.P. and H.D.; Methodology, O.P. and H.D.; Supervision, C.C.; Writing—original draft, O.P. and H.D.; Writing—review and editing, C.C. All authors have read and agreed to the published version of the manuscript.

Funding: The AvaSpec spectroradiometer was first purchased in the frame of the Research Unit "Integrated Geo-Characterisation of Aerosols" (GAIA, CUP code: B36G15002270006), which was partly funded by the European Regional Development Fund and the European Social Fund.

Data Availability Statement: The data from the ancillary instrumentation are publicly available from their respective international networks (e.g., aerosol optical and microphysical properties: Skynet, https://www.skynet-isdc.org/data.php, accessed on 23 March 2023; column ozone: EUBREWNET, https://eubrewnet.aemet.es/eubrewnet, accessed on 23 March 2023). The Bentham spectra can be downloaded from the World Ozone and Ultraviolet Radiation Data Centre (WOUDC, https://woudc.org/data/products/, accessed on 23 March 2023). The spectra collected with the AvaSpec and with the CMP-21 pyranometer are available from the authors.

Acknowledgments: The authors are grateful to their colleagues S. Drigo and M. Pignet (ARPA Valle d'Aosta) for their technical assistance, A.M. Siani (University of Rome) for her comments and K. Papachristopoulou (National Observatory of Athens) for her valuable suggestions on radiative transfer models. The authors thank the three reviewers for their careful reading of the manuscript and their comments.

Conflicts of Interest: The authors declare no conflict of interest.

References

1. Seckmeyer, G.; Bais, A.; Bernhard, G.; Blumthaler, M.; Drüke, S.; Kiedron, P.; Lantz, K.; McKenzie, R.; Riechelmann, S.; Kouremeti, N.; et al. *Instruments to Measure Solar Ultraviolet Radiation Part 4: Array Spectroradiometers*; Technical Report 191; WMO/TD-No. 1538; World Meteorological Organization: Geneva, Switzerland, 2010.
2. González, J.A.; Calbó, J. Assessing Rapid Variability in Atmospheric Apparent Optical Depth with an Array Spectrometer System. *Remote Sens.* **2020**, *12*, 2917. [CrossRef]
3. Jäkel, E.; Wendisch, M.; Blumthaler, M.; Schmitt, R.; Webb, A.R. A CCD Spectroradiometer for Ultraviolet Actinic Radiation Measurements. *J. Atmos. Ocean. Tech.* **2007**, *24*, 449–462. [CrossRef]
4. Kosmopoulos, P.; Kazadzis, S.; Lagouvardos, K.; Kotroni, V.; Bais, A. Solar energy prediction and verification using operational model forecasts and ground-based solar measurements. *Energy* **2015**, *93*, 1918–1930. [CrossRef]
5. Perry, M.; Troccoli, A. Impact of a fire burn on solar irradiance and PV power. *Sol. Energy* **2015**, *114*, 167–173. [CrossRef]
6. Li, X.; Wagner, F.; Peng, W.; Yang, J.; Mauzerall, D.L. Reduction of solar photovoltaic resources due to air pollution in China. *Proc. Natl. Acad. Sci. USA* **2017**, *114*, 11867–11872. [CrossRef]
7. Belluardo, G.; Galleano, R.; Zaaiman, W.; Pravettoni, M.; Halwachs, M.; Fucci, R.; Drobisch, A.; Friederichs, M.; Haverkamp, E.; Phinikarides, A.; et al. Are the spectroradiometers used by the PV community ready to accurately measure the classification of solar simulators in a broader wavelength range? *Sol. Energy* **2018**, *173*, 558–565. [CrossRef]
8. Rao, R.R.; Mani, M.; Ramamurthy, P.C. An updated review on factors and their inter-linked influences on photovoltaic system performance. *Heliyon* **2018**, *4*, e00815. [CrossRef]
9. Khanum, K.K.; Rao, A.; Balaji, N.C.; Mani, M.; Ramamurthy, P.C. Performance evaluation for PV systems to synergistic influences of dust, wind and panel temperatures: Spectral insight. In Proceedings of the 2016 IEEE 43rd Photovoltaic Specialists Conference (PVSC), Portland, OR, USA, 5–10 June 2016; pp. 1715–1718. [CrossRef]
10. Abderrezek, M.; Fathi, M. Experimental study of the dust effect on photovoltaic panels' energy yield. *Sol. Energy* **2017**, *142*, 308–320. [CrossRef]
11. Ustun, T.S.; Nakamura, Y.; Hashimoto, J.; Otani, K. Performance analysis of PV panels based on different technologies after two years of outdoor exposure in Fukushima, Japan. *Renew. Energ.* **2019**, *136*, 159–178. [CrossRef]
12. Sierk, B.; Bürki, B.; Becker-Ross, H.; Florek, S.; Neubert, R.; Kruse, L.P.; Kahle, H.G. Tropospheric water vapor derived from solar spectrometer, radiometer, and GPS measurements. *J. Geophys. Res.* **1997**, *102*, 22411–22424. [CrossRef]
13. Vandaele, A.C.; Fayt, C.; Hendrick, F.; Hermans, C.; Humbled, F.; Van Roozendael, M.; Gil, M.; Navarro, M.; Puentedura, O.; Yela, M.; et al. An intercomparison campaign of ground-based UV-visible measurements of NO_2, BrO, and OClO slant columns: Methods of analysis and results for NO_2. *J. Geophys. Res.* **2005**, *110*, D08305. [CrossRef]
14. Somieski, A.; Buerki, B.; Geiger, A.; Kahle, H.G.; Pavlis, E.C.; Becker-Ross, H.; Florek, S.; Okruss, M. Tropospheric water vapor from solar spectrometry and comparison with Jason microwave radiometer measurements. *J. Geophys. Res.* **2006**, *111*, D09104. [CrossRef]
15. Herman, J.; Cede, A.; Spinei, E.; Mount, G.; Tzortziou, M.; Abuhassan, N. NO_2 column amounts from ground-based Pandora and MFDOAS spectrometers using the direct-sun DOAS technique: Intercomparisons and application to OMI validation. *J. Geophys. Res.* **2009**, *114*, D13307. [CrossRef]
16. Bohn, B.; Lohse, I. Calibration and evaluation of CCD spectroradiometers for ground-based and airborne measurements of spectral actinic flux densities. *Atmos. Meas. Tech.* **2017**, *10*, 3151–3174. [CrossRef]
17. Raptis, P.I.; Kazadzis, S.; Gröbner, J.; Kouremeti, N.; Doppler, L.; Becker, R.; Helmis, C. Water vapour retrieval using the Precision Solar Spectroradiometer. *Atmos. Meas. Tech.* **2018**, *11*, 1143–1157. [CrossRef]
18. García-Cabrera, R.D.; Cuevas-Agulló, E.; Barreto, A.; Cachorro, V.E.; Pó, M.; Ramos, R.; Hoogendijk, K. Aerosol retrievals from the EKO MS-711 spectral direct irradiance measurements and corrections of the circumsolar radiation. *Atmos. Meas. Tech.* **2020**, *13*, 2601–2621. [CrossRef]

19. Naethe, P.; Delaney, M.; Julitta, T. Changes of NOx in urban air detected with monitoring VIS-NIR field spectrometer during the coronavirus pandemic: A case study in Germany. *Sci. Total Environ.* **2020**, *748*, 141286. [CrossRef] [PubMed]
20. García, R.D.; Cuevas, E.; Cachorro, V.E.; García, O.E.; Barreto, A.; Almansa, A.F.; Romero-Campos, P.M.; Ramos, R.; Pó, M.; Hoogendijk, K.; et al. Water Vapor Retrievals from Spectral Direct Irradiance Measured with an EKO MS-711 Spectroradiometer—Intercomparison with Other Techniques. *Remote Sens.* **2021**, *13*, 350. [CrossRef]
21. Zuber, R.; Köhler, U.; Egli, L.; Ribnitzky, M.; Steinbrecht, W.; Gröbner, J. Total ozone column intercomparison of Brewers, Dobsons, and BTS-Solar at Hohenpeißenberg and Davos in 2019/2020. *Atmos. Meas. Tech.* **2021**, *14*, 4915–4928. [CrossRef]
22. Ylianttila, L.; Visuri, R.; Huurto, L.; Jokela, K. Evaluation of a Single-monochromator Diode Array Spectroradiometer for Sunbed UV-radiation Measurements. *Photochem. Photobiol.* **2005**, *81*, 333–341. [CrossRef]
23. Coleman, A.; Sarkany, R.; Walker, S. Clinical ultraviolet dosimetry with a CCD monochromator array spectroradiometer. *Phys. Med. Biol.* **2008**, *53*, 5239. [CrossRef] [PubMed]
24. Kokhanovsky, A.; Di Mauro, B.; Garzonio, R.; Colombo, R. Retrieval of Dust Properties from Spectral Snow Reflectance Measurements. *Front. Environ. Sci.* **2021**, *9*, 644551. [CrossRef]
25. Wagner, A.; Hilgert, S.; Kattenborn, T.; Fuchs, S. Proximal VIS-NIR spectrometry to retrieve substance concentrations in surface waters using partial least squares modelling. *Water Supply* **2018**, *19*, 1204–1211. [CrossRef]
26. Cesana, I.; Bresciani, M.; Cogliati, S.; Giardino, C.; Gupana, R.; Manca, D.; Santabarbara, S.; Pinardi, M.; Austoni, M.; Lami, A.; et al. Preliminary Investigation on Phytoplankton Dynamics and Primary Production Models in an Oligotrophic Lake from Remote Sensing Measurements. *Sensors* **2021**, *21*, 5072. [CrossRef]
27. Maier, P.M.; Keller, S.; Hinz, S. Deep Learning with WASI Simulation Data for Estimating Chlorophyll a Concentration of Inland Water Bodies. *Remote Sens.* **2021**, *13*, 718. [CrossRef]
28. Suga, S.; Blattner, P.; Cordo, O.; Cornell, G.; Francis, A.; Habte, A.; Jung, J.; Kita, H.; Myers, D.; Regan, J.; et al. *Recommended Reference Solar Spectra for Industrial Applications*; CIE-International Commission on Illumination: Vienna, Austria, 2020. [CrossRef]
29. Bosch Ojeda, C.; Sánchez Rojas, F. Process Analytical Chemistry: Applications of Ultraviolet/Visible Spectrometry in Environmental Analysis: An Overview. *Appl. Spectrosc. Rev.* **2009**, *44*, 245–265. [CrossRef]
30. Zong, Y.; Brown, S.W.; Johnson, B.C.; Lykke, K.R.; Ohno, Y. Simple spectral stray light correction method for array spectroradiometers. *Appl. Opt.* **2006**, *45*, 1111–1119. [CrossRef]
31. Schinke, C.; Franke, M.; Bothe, K.; Nevas, S. Implementation and uncertainty evaluation of spectral stray light correction by Zong's method. *Appl. Opt.* **2019**, *58*, 9998–10009. [CrossRef]
32. Gröbner, J. *ENV03 Solar UV–Final Publishable JRP Report*; Technical Report; EURAMET: Brunswick, Germany, 2015.
33. Federico, S.; Torcasio, R.C.; Sanò, P.; Casella, D.; Campanelli, M.; Meirink, J.F.; Wang, P.; Vergari, S.; Diémoz, H.; Dietrich, S. Comparison of hourly surface downwelling solar radiation estimated from MSG–SEVIRI and forecast by the RAMS model with pyranometers over Italy. *Atmos. Meas. Tech.* **2017**, *10*, 2337–2352. [CrossRef]
34. Di Mauro, B.; Garzonio, R.; Rossini, M.; Filippa, G.; Pogliotti, P.; Galvagno, M.; Morra di Cella, U.; Migliavacca, M.; Baccolo, G.; Clemenza, M.; et al. Saharan dust events in the European Alps: Role in snowmelt and geochemical characterization. *Cryosphere* **2019**, *13*, 1147–1165. [CrossRef]
35. Terzago, S.; Andreoli, V.; Arduini, G.; Balsamo, G.; Campo, L.; Cassardo, C.; Cremonese, E.; Dolia, D.; Gabellani, S.; von Hardenberg, J.; et al. Sensitivity of snow models to the accuracy of meteorological forcings in mountain environments. *Hydrol. Earth Syst. Sci.* **2020**, *24*, 4061–4090. [CrossRef]
36. Fasano, G.; Diémoz, H.; Fountoulakis, I.; Cassardo, C.; Kudo, R.; Siani, A.M.; Ferrero, L. Vertical profile of the clear-sky aerosol direct radiative effect in an Alpine valley, by the synergy of ground-based measurements and radiative transfer simulations. *Bull. of Atmos. Sci. Technol.* **2021**, *2*, 11. [CrossRef]
37. Siani, A.M.; Casale, G.R.; Diémoz, H.; Agnesod, G.; Kimlin, M.G.; Lang, C.A.; Colosimo, A. Personal UV exposure in high albedo alpine sites. *Atmos. Chem. Phys.* **2008**, *8*, 3749–3760. [CrossRef]
38. Casale, G.R.; Siani, A.M.; Diémoz, H.; Agnesod, G.; Parisi, A.V.; Colosimo, A. Extreme UV index and solar exposures at Plateau Rosà (3500 ma.s.l.) in Valle d'Aosta Region, Italy. *Sci. Total Environ.* **2015**, *512–513*, 622–630. [CrossRef]
39. Manara, V.; Stocco, E.; Brunetti, M.; Diolaiuti, G.A.; Fugazza, D.; Pfeifroth, U.; Senese, A.; Trentmann, J.; Maugeri, M. Comparison of Surface Solar Irradiance from Ground Observations and Satellite Data (1990–2016) over a Complex Orography Region (Piedmont—Northwest Italy). *Remote Sens.* **2020**, *12*, 3882. [CrossRef]
40. Fountoulakis, I.; Diémoz, H.; Siani, A.M.; Laschewski, G.; Filippa, G.; Arola, A.; Bais, A.F.; De Backer, H.; Lakkala, K.; Webb, A.R.; et al. Solar UV Irradiance in a Changing Climate: Trends in Europe and the Significance of Spectral Monitoring in Italy. *Environments* **2020**, *7*, 1. [CrossRef]
41. Fountoulakis, I.; Diémoz, H.; Siani, A.M.; di Sarra, A.; Meloni, D.; Sferlazzo, D.M. Variability and trends in surface solar spectral ultraviolet irradiance in Italy: On the influence of geopotential height and lower-stratospheric ozone. *Atmos. Chem. Phys.* **2021**, *21*, 18689–18705. [CrossRef]
42. Eleftheratos, K.; Kapsomenakis, J.; Fountoulakis, I.; Zerefos, C.S.; Jöckel, P.; Dameris, M.; Bais, A.F.; Bernhard, G.; Kouklaki, D.; Tourpali, K.; et al. Ozone, DNA-active UV radiation, and cloud changes for the near-global mean and at high latitudes due to enhanced greenhouse gas concentrations. *Atmos. Chem. Phys.* **2022**, *22*, 12827–12855. [CrossRef]

43. Lakkala, K.; Kujanpää, J.; Brogniez, C.; Henriot, N.; Arola, A.; Aun, M.; Auriol, F.; Bais, A.F.; Bernhard, G.; De Bock, V.; et al. Validation of the TROPOspheric Monitoring Instrument (TROPOMI) surface UV radiation product. *Atmos. Meas. Tech.* **2020**, *13*, 6999–7024. [CrossRef]
44. Vitt, R.; Laschewski, G.; Bais, A.F.; Diémoz, H.; Fountoulakis, I.; Siani, A.M.; Matzarakis, A. UV-Index Climatology for Europe Based on Satellite Data. *Atmosphere* **2020**, *11*, 727. [CrossRef]
45. Kosmopoulos, P.G.; Kazadzis, S.; Schmalwieser, A.W.; Raptis, P.I.; Papachristopoulou, K.; Fountoulakis, I.; Masoom, A.; Bais, A.F.; Bilbao, J.; Blumthaler, M.; et al. Real-time UV index retrieval in Europe using Earth observation-based techniques: System description and quality assessment. *Atmos. Meas. Tech.* **2021**, *14*, 5657–5699. [CrossRef]
46. Diémoz, H.; Magri, T.; Pession, G.; Tarricone, C.; Tombolato, I.K.F.; Fasano, G.; Zublena, M. Air Quality in the Italian Northwestern Alps during Year 2020: Assessment of the COVID-19 «Lockdown Effect» from Multi-Technique Observations and Models. *Atmosphere* **2021**, *12*, 1006. [CrossRef]
47. Diémoz, H.; Egli, L.; Gröbner, J.; Siani, A.M.; Diotri, F. Solar ultraviolet irradiance measurements in Aosta (Italy): An analysis of short- and middle-term spectral variability. *AIP Conf. Proc.* **2013**, *1531*, 856–859. [CrossRef]
48. Kouremeti, N.; Bais, A.; Kazadzis, S.; Blumthaler, M.; Schmitt, R. Charge-coupled device spectrograph for direct solar irradiance and sky radiance measurements. *Appl. Opt.* **2008**, *47*, 1594–1607. [CrossRef]
49. Hooke, R.; Pearson, A.; O'Hagan, J. Autonomous Portable Solar Ultraviolet Spectroradiometer (APSUS)–A New CCD Spectrometer System for Localized, Real-Time Solar Ultraviolet (280–400 nm) Radiation Measurement. *Photochem. Photobiol.* **2014**, *90*, 903–910. [CrossRef]
50. Price, L.L.A.; Hooke, R.J.; Khazova, M. Effects of ambient temperature on the performance of CCD array spectroradiometers and practical implications for field measurements. *J. Radiol. Prot.* **2014**, *34*, 655. [CrossRef]
51. Ylianttila, L.; Schreder, J. Temperature effects of PTFE diffusers. *Opt. Mater.* **2005**, *27*, 1811–1814. [CrossRef]
52. Baczynska, K.A.; Khazova, M. Methods of dark signal determination for CCD array spectroradiometers used in solar UVR measurements. *Radiat. Prot. Dosim.* **2014**, *163*, 387–393. [CrossRef]
53. Diémoz, H.; Siani, A.M.; Casale, G.R.; di Sarra, A.; Serpillo, B.; Petkov, B.; Scaglione, S.; Bonino, A.; Facta, S.; Fedele, F.; et al. First national intercomparison of solar ultraviolet radiometers in Italy. *Atmos. Meas. Tech.* **2011**, *4*, 1689–1703. [CrossRef]
54. Fountoulakis, I.; Diémoz, H.; Siani, A.M.; Hülsen, G.; Gröbner, J. Monitoring of solar spectral ultraviolet irradiance in Aosta, Italy. *Earth Syst. Sci. Data* **2020**, *12*, 2787–2810. [CrossRef]
55. Hülsen, G.; Gröbner, J.; Nevas, S.; Sperfeld, P.; Egli, L.; Porrovecchio, G.; Smid, M. Traceability of solar UV measurements using the Qasume reference spectroradiometer. *Appl. Opt.* **2016**, *55*, 7265–7275. [CrossRef]
56. Siani, A.M.; Frasca, F.; Scarlatti, F.; Religi, A.; Diémoz, H.; Casale, G.R.; Pedone, M.; Savastiouk, V. Examination on total ozone column retrievals by Brewer spectrophotometry using different processing software. *Atmos. Meas. Tech.* **2018**, *11*, 5105–5123. [CrossRef]
57. Petkov, B.H.; Vitale, V.; Di Carlo, P.; Drofa, O.; Mastrangelo, D.; Smedley, A.R.D.; Diémoz, H.; Siani, A.M.; Fountoulakis, I.; Webb, A.R.; et al. An Unprecedented Arctic Ozone Depletion Event during Spring 2020 and Its Impacts Across Europe. *J. Geophys. Res. Atmos.* 2023, *128*, e2022JD037581. [CrossRef]
58. Diémoz, H.; Siani, A.M.; Redondas, A.; Savastiouk, V.; McElroy, C.T.; Navarro-Comas, M.; Hase, F. Improved retrieval of nitrogen dioxide (NO_2) column densities by means of MKIV Brewer spectrophotometers. *Atmos. Meas. Tech.* **2014**, *7*, 4009–4022. [CrossRef]
59. Diémoz, H.; Siani, A.M.; Casadio, S.; Iannarelli, A.M.; Casale, G.R.; Savastiouk, V.; Cede, A.; Tiefengraber, M.; Müller, M. Advanced NO_2 retrieval technique for the Brewer spectrophotometer applied to the 20-year record in Rome, Italy. *Earth Syst. Sci. Data* **2021**, *13*, 4929–4950. [CrossRef]
60. Diémoz, H.; Campanelli, M.; Estellés, V. One Year of Measurements with a POM-02 Sky Radiometer at an Alpine EuroSkyRad Station. *J. Meteorol. Soc. Jpn.* **2014**, *92A*, 1–16. [CrossRef]
61. Campanelli, M.; Iannarelli, A.M.; Mevi, G.; Casadio, S.; Diémoz, H.; Finardi, S.; Dinoi, A.; Castelli, E.; di Sarra, A.; Di Bernardino, A.; et al. A wide-ranging investigation of the COVID-19 lockdown effects on the atmospheric composition in various Italian urban sites (AER–LOCUS). *Urban Clim.* **2021**, *39*, 100954. [CrossRef]
62. Kudo, R.; Diémoz, H.; Estellés, V.; Campanelli, M.; Momoi, M.; Marenco, F.; Ryder, C.L.; Ijima, O.; Uchiyama, A.; Nakashima, K.; et al. Optimal use of the Prede POM sky radiometer for aerosol, water vapor, and ozone retrievals. *Atmos. Meas. Tech.* **2021**, *14*, 3395–3426. [CrossRef]
63. Davenport, J.J.; Hodgkinson, J.; Saffell, J.R.; Tatam, R.P. Noise analysis for CCD-based ultraviolet and visible spectrophotometry. *Appl. Opt.* **2015**, *54*, 8135–8144. [CrossRef]
64. Cede, A. *Manual for Blick Software Suite 1.8*; Manual Version 1.8-4; LuftBlick: Innsbruck, Austria, 2021.
65. Pulli, T.; Nevas, S.; El Gawhary, O.; van den Berg, S.; Askola, J.; Kärhä, P.; Manoocheri, F.; Ikonen, E. Nonlinearity characterization of array spectroradiometers for the solar UV measurements. *Appl. Opt.* **2017**, *56*, 3077–3086. [CrossRef]
66. Kreuter, A.; Blumthaler, M. Stray light correction for solar measurements using array spectrometers. *Rev. Sci. Instrum.* **2009**, *80*, 096108. [CrossRef] [PubMed]
67. Wu, Z.; Dai, C.; Wang, Y.; Li, L. Stray light correction of array spectroradiometer measurement in ultraviolet. *J. Phys. Conf. Ser.* **2018**, *972*, 012022. [CrossRef]
68. Zuber, R.; Ribnitzky, M.; Tobar, M.; Lange, K.; Kutscher, D.; Schrempf, M.; Niedzwiedz, A.; Seckmeyer, G. Global spectral irradiance array spectroradiometer validation according to WMO. *Meas. Sci. Technol.* **2018**, *29*, 105801. [CrossRef]

69. Pavanello, D.; Galleano, R.; Zaaiman, W.; Ankit, M.; Kouremeti, N.; Gröbner, J.; Hoogendijk, K.; Po, M.; Lisbona, E.; Alius, W.; et al. Results of the IX International Spectroradiometer Intercomparison and impact on precise measurements of new photovoltaic technologies. *Prog. Photovolt. Res. Appl.* **2021**, *29*, 109–123. [CrossRef]
70. Slaper, H.; Reinen, H.A.J.M.; Blumthaler, M.; Huber, M.; Kuik, F. Comparing ground-level spectrally resolved solar UV measurements using various instruments: A technique resolving effects of wavelength shift and slit width. *Geophys. Res. Lett.* **1995**, *22*, 2721–2724. [CrossRef]
71. CIE. CIE S007/E-1998 Erythema reference action spectrum and standard erythema dose. *Color Res. Appl.* **1999**, *24*, 158. [CrossRef]
72. Emde, C.; Buras-Schnell, R.; Kylling, A.; Mayer, B.; Gasteiger, J.; Hamann, U.; Kylling, J.; Richter, B.; Pause, C.; Dowling, T.; et al. The libRadtran software package for radiative transfer calculations (version 2.0.1). *Geosci. Model Dev.* **2016**, *9*, 1647–1672. [CrossRef]
73. Ansko, I.; Eerme, K.; Lätt, S.; Noorma, M.; Veismann, U. Study of suitability of AvaSpec array spectrometer for solar UV field measurements. *Atmos. Chem. Phys.* **2008**, *8*, 3247–3253. [CrossRef]
74. Campanelli, M.; Mascitelli, A.; Sanò, P.; Diémoz, H.; Estellés, V.; Federico, S.; Iannarelli, A.M.; Fratarcangeli, F.; Mazzoni, A.; Realini, E.; et al. Precipitable water vapour content from ESR/SKYNET sun–sky radiometers: Validation against GNSS/GPS and AERONET over three different sites in Europe. *Atmos. Meas. Tech.* **2018**, *11*, 81–94. [CrossRef]
75. Coddington, O.M.; Richard, E.C.; Harber, D.; Pilewskie, P.; Woods, T.N.; Chance, K.; Liu, X.; Sun, K. The TSIS-1 Hybrid Solar Reference Spectrum. *Geophys. Res. Lett.* **2021**, *48*, e2020GL091709. [CrossRef]
76. Anderson, G.; Clough, S.; Kneizys, F.; Chetwynd, J.; Shettle, E. *Tech. Rep. AFGL-TR-86-0110*; Air Force Geophysics Laboratory: Bedford, MA, USA, 1986.
77. Bass, A.M.; Paur, R.J. The Ultraviolet Cross-Sections of Ozone: I. The Measurements. In *Atmospheric Ozone*; Springer: Dordrecht, The Netherlands, 1985; pp. 606–610.
78. Gies, P.; Hooke, R.; McKenzie, R.; O'Hagan, J.; Henderson, S.; Pearson, A.; Khazova, M.; Javorniczky, J.; King, K.; Tully, M.; et al. International Intercomparison of Solar UVR Spectral Measurement Systems in Melbourne in 2013. *Photochem. Photobiol.* **2015**, *91*, 1237–1246. [CrossRef] [PubMed]
79. Sildoja, M.M.; Nevas, S.; Kouremeti, N.; Gröbner, J.; Pape, S.; Pendsa, S.; Sperfeld, P.; Kemus, F. LED-based UV source for monitoring spectroradiometer properties. *Metrologia* **2018**, *55*, S97. [CrossRef]
80. Schinke, C.; Pollex, H.; Hinken, D.; Wolf, M.; Bothe, K.; Kröger, I.; Nevas, S.; Winter, S. Calibrating spectrometers for measurements of the spectral irradiance caused by solar radiation. *Metrologia* **2020**, *57*, 065027. [CrossRef]
81. Dirnberger, D.; Blackburn, G.; Müller, B.; Reise, C. On the impact of solar spectral irradiance on the yield of different PV technologies. *Sol. Energy Mater. Sol. Cells* **2015**, *132*, 431–442. [CrossRef]
82. Müllejans, H.; Ioannides, A.; Kenny, R.; Zaaiman, W.; Ossenbrink, H.A.; Dunlop, E.D. Spectral mismatch in calibration of photovoltaic reference devices by global sunlight method. *Meas. Sci. Technol.* **2005**, *16*, 1250. [CrossRef]
83. López Rodríguez, G.; Gueymard, C.; Polo, J.; Martín-Chivelet, N.; Alonso-Montesinos, J.; Marzo, A.; Batlles Garrido, F.; Vela, N.; Barbero, J. Assessing Spectral Mismatch Factors from Solar Spectral Measurements under Clear and Hazy Conditions. In Proceedings of the 36th European Photovoltaic Solar Energy Conference and Exhibition, Marseille, France, 9–13 September 2019; pp. 1374–1378. [CrossRef]
84. Kinsey, G.S. Spectrum Sensitivity, Energy Yield, and Revenue Prediction of PV Modules. *IEEE J. Photovolt.* **2015**, *5*, 258–262. [CrossRef]
85. Beć, K.B.; Grabska, J.; Huck, C.W. Principles and Applications of Miniaturized Near-Infrared (NIR) Spectrometers. *Chem.-Eur. J.* **2021**, *27*, 1514–1532. [CrossRef]
86. Krause, J.; Grüger, H.; Gebauer, L.; Zheng, X.; Knobbe, J.; Pügner, T.; Kicherer, A.; Gruna, R.; Längle, T.; Beyerer, J. SmartSpectrometer—Embedded Optical Spectroscopy for Applications in Agriculture and Industry. *Sensors* **2021**, *21*, 4476. [CrossRef] [PubMed]
87. Li, A.; Yao, C.; Xia, J.; Wang, H.; Cheng, Q.; Penty, R.; Fainman, Y.; Pan, S. Advances in cost-effective integrated spectrometers. *Light Sci. Appl.* **2022**, *11*, 174. [CrossRef] [PubMed]
88. Galleano, R.; Zaaiman, W.; Virtuani, A.; Pavanello, D.; Morabito, P.; Minuto, A.; Spena, A.; Bartocci, S.; Fucci, R.; Leanza, G.; et al. Intercomparison campaign of spectroradiometers for a correct estimation of solar spectral irradiance: Results and potential impact on photovoltaic devices calibration. *Prog. Photovolt. Res. Appl.* **2014**, *22*, 1128–1137. [CrossRef]
89. Galleano, R.; Zaaiman, W.; Strati, C.; Bartocci, S.; Pravettoni, M.; Marzoli, M.; Fucci, R.; Leanza, G.; Timò, G.; Minuto, A.; et al. Second international spectroradiometer intercomparison: Results and impact on PV device calibration. *Prog. Photovolt.* **2015**, *23*, 929–938. [CrossRef]
90. Pravettoni, M.; Galleano, R.; Jungst, G.; Balenzategui, J.; Bartocci, S.; Bogeat Sanchez-Piqueras, J.; Del Bolgia, M.; Fabero, F.; Fucci, R.; Gadermaier, J.; et al. Results of the fourth international spectral measurement intercomparison of a steady-state AM0 solar simulator. In Proceedings of the International PVSEC-25, Busan, Republic of Korea, 15–20 November 2015.
91. Egli, L.; Gröbner, J.; Hülsen, G.; Bachmann, L.; Blumthaler, M.; Dubard, J.; Khazova, M.; Kift, R.; Hoogendijk, K.; Serrano, A.; et al. Quality assessment of solar UV irradiance measured with array spectroradiometers. *Atmos. Meas. Tech.* **2016**, *9*, 1553–1567. [CrossRef]

92. Galleano, R.; Zaaiman, W.; Alonso-Álvarez, D.; Minuto, A.; Ferretti, N.; Fucci, R.; Pravettoni, M.; Halwachs, M.; Friederichs, M.; Plag, F.; et al. Results of the Fifth International Spectroradiometer Comparison for Improved Solar Spectral Irradiance Measurements and Related Impact on Reference Solar Cell Calibration. *IEEE J. Photovolt.* **2016**, *6*, 1587–1597. [CrossRef]
93. Galleano, R.; Pavanello, D.; Zaaiman, W.; Jungst, G.; Halwachs, M.; Rennhofer, M.; Alejo, A.; Haverkamp, E.; Van der Woude, D.; Minuto, A. Spectroradiometer Comparison under Outdoor Direct Normal Irradiance and Indoor High-Power AM0-Like Conditions. In Proceedings of the 36th European PVSEC, Marseille, France, 9–13 September 2019; pp. 1460–1465. [CrossRef]
94. González, C.; Vilaplana, J.M.; Bogeat, J.A.; Serrano, A. Comparison of global UV spectral irradiance measurements between a BTS CCD-array and a Brewer spectroradiometer. *Atmos. Meas. Tech.* **2022**, *15*, 4125–4133. [CrossRef]